IEEE Access
Multidisciplinary | Rapid Review | Open Access Journal

Received 3 February 2026, accepted 18 February 2026, date of publication 2 March 2026, date of current version 5 March 2026.

Digital Object Identifier 10.1109/ACCESS.2026.3669094

RESEARCH ARTICLE

Exhaustive Structure Learning of R-Vine Copula Models for Analyzing Multiband Spectrum Utilization in Mobile Communications

YUNBAE KIM, JONGHUN YOON, HYEYEON KWON, AND SEUNGKEUN PARK, (Member, IEEE)
Electronics and Telecommunications Research Institute, Yuseong-gu, Daejeon 34129, Republic of Korea
Corresponding author: Yunbae Kim (doko9gum@etri.re.kr)

This work was supported by the Institute for Information & Communications Technology Promotion (IITP) grant funded by the Korea Government (MSIT) (No. 2021-0-00092, Development of Technology for Securing and Supplying Spectrum Resources).

ABSTRACT Accurate modeling of multiband spectrum utilization is essential for data-driven spectrum management and refarming in mobile communication systems. However, the bounded and non-Gaussian nature of Resource Block (RB) utilization, together with complex inter-band dependencies, challenges conventional multivariate modeling approaches. This work proposes a flexible density estimation framework based on Regular vine (R-vine) copulas, which construct joint distributions from bivariate components. Since practical LTE and 5G deployments involve only a small number of concurrently used bands, we perform an exhaustive search over all admissible R-vine structures to identify the optimal dependence configuration. To support this search, we develop an efficient enumeration algorithm that incrementally constructs valid edge sets while directly enforcing the proximity condition. For each pair-copula term, we adopt Gaussian Mixture Copula Models to capture complex and nonparametric dependence patterns, and we derive gradient expressions that enable efficient likelihood-based parameter estimation. The proposed framework is validated using real-world LTE measurements of multiband RB utilization. Goodness-of-fit evaluations confirm that the estimated distributions accurately reflect observed patterns, while the learned dependence structures reveal interpretable inter-band behaviors, preferential usage relationships, and band-specific load characteristics. These results demonstrate the suitability of flexible copula-based modeling, particularly in low-dimensional settings relevant to simulation-driven spectrum planning in modern communication systems.

INDEX TERMS Gaussian mixture copula models, mobile communication networks, multivariate density estimation, spectrum utilization analysis, vine copulas.

I. INTRODUCTION

Low-frequency spectrum resources play a critical role in mobile communication systems due to their favorable propagation characteristics, including wide-area coverage and strong indoor penetration [1]. Even with the evolution toward next-generation networks such as 5G and beyond, the demand for these low-frequency bands remains high. As a result, the low-frequency spectrum currently occupied by legacy Long-Term Evolution (LTE) systems must be reassessed to determine its suitability for reclamation and refarming for future services [2]. Modern LTE deployments utilize multiple fragmented bands, each offering distinct coverage and capacity characteristics depending on frequency [3]. Identifying which of these bands may be considered for reallocation requires an understanding of how spectrum resources are currently utilized across frequency bands.

In multiband LTE deployments, analyzing how utilization across bands varies together is essential for understanding their operational roles and interactions. Such information can be derived from the downlink control channel signals transmitted by operational LTE Base Stations (BSs) [4]. However, the amount and diversity of multiband spectrum usage data that can be collected through measurement campaigns are

The associate editor coordinating the review of this manuscript and approving it for publication was Yiming Tang.

inherently limited, and large-scale data acquisition is costly and resource-intensive. To support tasks such as spectrum planning, traffic forecasting, and scenario-based simulation, it is therefore necessary to estimate the underlying probability distribution governing multiband spectrum usage. These challenges call for flexible multivariate density estimation methods capable of modeling latent dependency structures and supporting simulation-based spectrum planning [5].

In our analysis, spectrum usage in each band is quantified by Resource Block (RB) utilization–a fundamental allocation unit in both 4G and 5G systems. For each band, the total number of RBs is determined by its allocated bandwidth, and utilization is defined as the proportion of RBs in use, yielding marginal variables that are naturally bounded within [0, 1]. Because of this bounded support and the empirically non-Gaussian behavior of RB utilization, classical parametric distributions often fail to provide sufficient modeling flexibility [6]. These challenges become even more pronounced in the multivariate setting, where accurately representing inter-band dependencies is essential for realistic modeling of multiband spectrum usage.

To address the need for flexible multivariate modeling, we adopt a copula-based framework. Copulas allow the joint distribution to be constructed by modeling marginal behaviors and dependence structures separately, as established by Sklar's theorem [7]. While a wide variety of parametric families exist for bivariate copulas, extending such models directly to higher dimensions is generally infeasible due to limited flexibility and structural constraints [8]. Vine copulas overcome this limitation by composing multivariate dependence structures from a cascade of bivariate building blocks [9]. A vine is a nested sequence of trees that encodes conditional dependencies among variables, and the class of Regular vines (R-vines) provides a highly expressive and interpretable framework for constructing multivariate distributions [10].

The expressive power of an R-vine copula is determined by its underlying vine structure, which specifies the sequence of conditional dependencies among variables. Because the number of admissible R-vine structures grows rapidly with the number of variables, specifically as $\frac{d!}{2} \times 2^{\binom{d-2}{2}}$ for d variables [11], identifying an appropriate structure has been an active area of research. In [12], a tree-by-tree approach was proposed that greedily finds a spanning tree that maximizes the sum of absolute pairwise dependencies at each level. This method is effective for low-dimensional problems, but the greedy approach does not guarantee optimal solutions for high-dimensional cases. For higher-dimensional data, various methods have been proposed to effectively explore all possible vine structures. In [13] and [14], a Bayesian approach utilizing reversible jump Markov Monte Carlo posterior simulation is proposed. In [15], a vine structure learning problem is formulated as a sequential decision-making problem based on reinforcement learning. In this approach, each decision corresponds to a decision of an edge and a corresponding bivariate copula.

In practical mobile network deployments, the number of concurrently utilized frequency bands that require dependence modeling is typically small, typically ranges from five to six. This is because current 4G and 5G systems operate over a limited set of fragmented bands, and ongoing refarming as well as regulatory harmonization efforts are expected to further consolidate these bands over time [16]. Consequently, the dimensionality of jointly used bands remains low. Under these conditions, exhaustive exploration of all admissible R-vine structures becomes not only feasible but also desirable, as it enables more accurate identification of the optimal dependence representation than methods designed primarily for high-dimensional scenarios.

Motivated by this observation, we develop a complete modeling framework that performs exhaustive search over the full set of valid R-vine structures. To support this process, we introduce an enumeration algorithm that constructs candidate edge sets by directly enforcing proximity conditions at each vine level. In contrast to approaches that rely on spanning-tree enumeration [12], [14], the proposed method eliminates unnecessary combinatorial overhead while ensuring structural validity throughout the construction process.

For each edge representing a bivariate dependence, we adopt the Gaussian Mixture Copula Model (GMCM) [17], which provides an expressive nonparametric alternative to standard copula families. GMCM parameters are estimated using gradient-based likelihood maximization, supported by analytically derived gradient expressions that facilitate efficient and stable optimization. By combining exhaustive structure search with this flexible modeling approach, the proposed framework aims to improve estimation accuracy relative to methods that rely on fixed parametric bivariate families [12], [13], [14], [15].

We apply the proposed modeling framework to real-world LTE measurements that capture multiband RB utilization. To evaluate the statistical validity of the learned distribution, we perform goodness-of-fit tests, confirming that the model accurately represents the observed multiband usage patterns. Building on this validated model, we conduct a detailed analysis of LTE spectrum utilization. This includes examining inter-band dependency structures to infer the functional roles of individual frequency bands and identifying characteristic joint usage behaviors. We further compute the probability that RB utilization in one band exceeds that of others, enabling quantitative assessment of preferential usage trends. In addition, we estimate cell-site traffic load distributions by incorporating spectral efficiency and bandwidth information, thereby supporting realistic Monte Carlo simulations and data-driven spectrum refarming decisions.

The main contributions of this work are summarized as follows:

- We propose a full exhaustive-search algorithm for identifying optimal R-vine structures tailored to low-dimensional multiband spectrum usage.

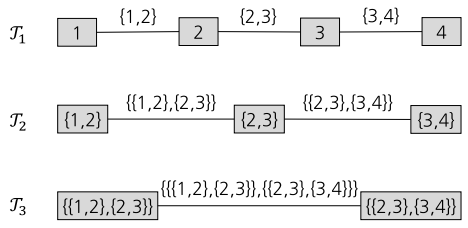

(a) A drawable vine on 4 elements

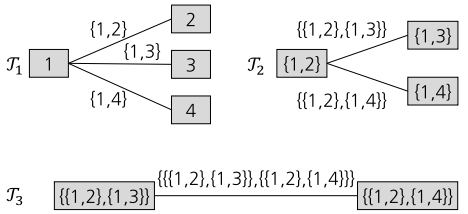

(b) A canonical vine on 4 elements

FIGURE 1. The two boundary cases of R-vines on four elements.

- We introduce a GMCM-based bivariate copula estimation method with derived gradient expressions, enabling accurate and flexible dependence modeling.
- We construct a multivariate probabilistic model for LTE multiband RB utilization and validate it using real measurement data through statistical goodness-of-fit tests.
- We demonstrate practical spectrum utilization analyses, including dependency characterization, preferential band usage assessment, and cell traffic load estimation to support simulation-based spectrum planning.

The remainder of this paper is organized as follows. Sections II and III present the background on R-vines and GMCMs. Section IV describes the proposed learning framework. Section V reports experimental results using measured LTE RB usage data. Section VI provides spectrum utilization analyses based on the estimated distribution. Finally, Section VII concludes this work.

II. VINE COPULAS AND MULTIVARIATE MODELING

In this section, we summarize what a vine structure is and how it models dependencies between variables to form a multivariate probability distribution. A detailed explanation can be found in [18] and [19].

Let $\mathcal{N} = \{1, 2, \ldots, d\}$ be a set of d nodes. A *vine* on $\mathcal{N}$ is defined as a sequence of nested trees $\mathcal{V} = \{\mathcal{T}_1, \ldots, \mathcal{T}_{d-1}\}$, where each tree $\mathcal{T}_j$ consists of a set of nodes $\mathcal{N}_j$ and a set of edges $\mathcal{E}_j$ such that:

- $\mathcal{T}_1$ is a tree with node set $\mathcal{N}_1 = \mathcal{N}$ and edge set $\mathcal{E}_1$;
- For $j = 2, \ldots, d-1$, $\mathcal{T}_j$ is a tree whose nodes correspond to the edges of $\mathcal{T}_{j-1}$, i.e., $\mathcal{N}_j = \mathcal{E}_{j-1}$.

The complete edge set of the vine is denoted as $\mathcal{E}(\mathcal{V}) = \mathcal{E}_1 \cup \cdots \cup \mathcal{E}_{d-1}$. The vine is called an R-vine if it additionally satisfies the *proximity* condition: for any edge $\{a, b\} \in \mathcal{E}_j$ with $j \geq 2$, $|a \triangle b| = 2$ where $\triangle$ denotes the symmetric difference of sets and $|\cdot|$ denotes the cardinality. This condition ensures that an edge between two nodes in $\mathcal{T}_j$ is allowed only if the corresponding edges in $\mathcal{T}_{j-1}$ share a common node. This condition provides the structural foundation for defining valid conditional dependencies in higher-order trees.

Figure 1 illustrates two canonical examples of R-vines on four elements.

As seen in the figure, explicit set-based representation of nodes and edges becomes complex as the vine depth increases. To simplify notation, we define the complete union U_e of an edge $e \in \mathcal{E}_i$ recursively as

$$U_e = \big\{a \in \mathcal{N}_1 | \exists e_j \in \mathcal{E}_j \text{ for } 1 \leq j \leq i-1 \text{ such that } a \in e_1 \in \cdots \in e_{i-1} \in e\big\}.$$

That is, U_e collects all original variables involved in the recursive chain leading to e. Also, for an edge $e = \{a, b\}$, we define the conditioning set as $S_e = U_a \cap U_b$ and the conditioned set as $U_a \triangle U_b$. In the base tree $\mathcal{T}_1$, we have $S_e = \emptyset$. With this formulation, we have the following useful properties for R-vines.

Proposition 1: Let $\mathcal{V}$ be an R-vine on d elements.

1) For any $e \in \mathcal{E}_i$, $i = 1, \ldots, d-1$, $|U_e| = i + 1$,
2) For $e = \{a, b\}$, $U_a \setminus S_e$ and $U_b \setminus S_e$ are singletons, and hence, the conditioned set associated with e is a doubleton and $|S_e| = i - 1$,
3) For $e = \{a, b\}$, if an element $j \in \mathcal{N}_1$ is a member of the conditioned set associated with e, then j is a member of the conditioned set associated with exactly one of a and b, and S_a and S_b are subsets of S_e,
4) Every pair of elements occurs exactly once as the conditioned set of an edge.

Proof: Properties 1), 2), and 3) follow from Lemmas 4.2, 4.3, and 4.6 in [20], respectively. For property 4), Lemma 4.5 in [20] states that if two edges have the same conditioned set, then the edges themselves must be equal. Since an R-vine on d elements consists of exactly $\binom{d}{2}$ edges, each pair of elements occurs exactly once as the conditioned set of an edge. ■

From the second one of Proposition 1, for $e = \{a, b\}$, we can abbreviate the representation as $(a_e, b_e; S_e)$ where $\{a_e\} = U_a \setminus S_e$ and $\{b_e\} = U_b \setminus S_e$. For example, the edge $e = \{\{1, 2\}, \{2, 3\}\}, \{\{2, 3\}, \{3, 4\}\}\}$ of $\mathcal{T}_3$ in Figure 1-(a) has $a = \{\{1, 2\}, \{2, 3\}\}$, $b = \{\{2, 3\}, \{3, 4\}\}$, $S_e = \{2, 3\}$, $a_e = 1$, and $b_e = 4$. It follows that $e = (1, 4; \{2, 3\})$ or $e = (1, 4; 2, 3)$.

When utilizing vine structures for modeling multivariate probability distributions, each edge is associated with a bivariate copula. Each bivariate copula captures the dependence between two variables or conditional variables. According to Sklar's theorem [7], any continuous bivariate distribution function H with margins F and G admits a unique copula C such that:

$$H(x, y) = C(F(x), G(y)). \tag{1}$$

Conversely, combining any pair of marginal distributions F and G with a copula C via (1) yields a valid joint distribution. This result allows one to express any bivariate distribution as a composition of its marginals and a bivariate copula capturing the dependence structure. Note that every bivariate copula is a restriction to $[0, 1]^2$ of a joint distribution whose margins are continuous uniform distributions on $(0, 1)$.

Conditional distributions play a key role in the vine copula construction. Partial derivatives of copulas can be used to derive conditional distributions. Let (U, V) be a pair of random variables uniformly distributed on $(0, 1)$ whose joint distribution function is C. Then the conditional distribution function for V given $U = u$, which we denote $C(v|u)$, is given by

$$C(v|u) = P(V \le v|U = u) = \frac{\partial C(u, v)}{\partial u}. \tag{2}$$

An R-vine distribution for a d-dimensional random vector $(X_1, \ldots, X_d)$ is specified by a triplet $(\mathcal{F}, \mathcal{V}, \mathcal{B})$, where:

- $\mathcal{F} = (F_1, \ldots, F_d)$ is the vector of the marginal distributions;
- $\mathcal{V}$ is an R-vine structure;
- $\mathcal{B} = \{C_e | e \in \mathcal{E}(\mathcal{V})\}$ is the set of bivarate copulas assigned to edges.

Each variable X_i is assumed to have a density f_i for $1 \le i \le d$, and each copula C_e is assumed to have an associated density c_e for $e \in \mathcal{E}(\mathcal{V})$. For an edge $e = \{a, b\} = (a, b; \emptyset) \in \mathcal{E}_1$, C_e is a bivariate distribution of $(F_a(X_a), F_b(X_b))$. The copulas associated with the edges of the higher-order trees are applied to conditional distributions. Specifically, for an edge $e = (a_e, b_e; S_e) \in \mathcal{E}_j$, $j = 2, \ldots, d-1$, the copula C_e is associated with the conditional distributions of X_{a_e} and X_{b_e} given X_i's for $i \in S_e$. In fact, such a distribution depends on the realized values of conditioning variables X_i's for $i \in S_e$. To reduce complexity and computational burden involved in estimating copulas, we normally neglect the dependence on the specific conditioning values. In this regard, the *simplifying assumption* is made that the copula for each edge depends only on the variables associated with it, not its values.

Given the triplet $(\mathcal{F}, \mathcal{V}, \mathcal{B})$ defined above, the induced multivariate distribution admits the density given in (3), as shown at the bottom of the page. The last term in (3) contains conditional distributions for multidimensional variables. As in the bivariate case, an n-variate copula is the joint distribution of a random vector whose marginals are uniform on $(0, 1)$. For any edge $e = (a_e, b_e; S_e) \in \mathcal{E}_j, j = 2, \ldots, d-1$, we have

$$F_{a_e|S_e}\left(x_{a_e}|x_j, j \in S_e\right) = C_{a_e|S_e}\left(F_{a_e}(x_{a_e})|F_j(x_j), j \in S_e\right), \tag{4}$$

where $C_{a_e|S_e}$ is the conditional distribution of $F_{a_e}(X_{a_e})$ given $F_j(X_j)$s for $j \in S_e$. Fortunately, this can be obtained sequentially from the bivariate copulas associated with the edges of the lower-order trees. For an edge $e = \{a, b\} \in \mathcal{E}_1$, the conditional copulas $C_{a|b}$ and $C_{b|a}$ are obtained from the partial derivatives of $C_{a,b}$ as in (2). For an edge $e = (a_e, b_e; S_e) \in \mathcal{E}_j, j = 2, \ldots, d-2$, let the conditional distributions $C_{a_e|S_e}$ and $C_{b_e|S_e}$ be given. The conditional distribution $C_{a_e|S_e \cup \{b_e\}}$ that can be used for copulas associated with the edges of the next level tree can be obtained as shown in (5), as shown at the bottom of the next page. In (5), the term $C_{a_e|b_e;S_e}$ denotes the conditional copula obtained from $C_{a_e,b_e;S_e}$ using (2).

III. GAUSSIAN MIXTURE COPULA MODEL

As discussed in Section II, an R-vine copula constructs a multivariate distribution entirely from bivariate copulas. Consequently, the overall expressiveness of the vine copula model depends critically on the flexibility of its bivariate components. While many standard bivariate copulas are available, they often lack the capacity to represent complex or multimodal dependencies. One way to enhance modeling flexibility is to employ mixture-based formulations [6].

In this regard, [17] introduced the GMCM, which combines the flexibility of mixture models with the modularity of copula theory by decoupling marginal behavior from dependence structure. In the GMCM framework, dependence is captured using a Gaussian Mixture Model (GMM), while marginal distributions are treated separately. In this section, we briefly introduce how the Gaussian mixture copula function is defined for two variables.

Let (Y_1, Y_2) be a bivariate random vector modeled by a K-component GMM, $f(y_1, y_2) = \sum_{k=1}^{K} \pi_k \phi(y_1, y_2; \boldsymbol{\mu}_k, \boldsymbol{\Sigma}_k)$, where the weights $\pi_k \ge 0$ satisfy $\sum_{k=1}^{K} \pi_k = 1$. The function $\phi(\cdot, \cdot; \boldsymbol{\mu}_k, \boldsymbol{\Sigma}_k)$ denotes the bivariate Gaussian density with mean vector $\boldsymbol{\mu}_k = [\mu_{k1}, \mu_{k2}]^\top$ and covariance matrix $\boldsymbol{\Sigma}_k = \begin{bmatrix} \sigma_{k1}^2 & \rho_k \sigma_{k1} \sigma_{k2} \\ \rho_k \sigma_{k1} \sigma_{k2} & \sigma_{k2}^2 \end{bmatrix}$, whose analytic form is given in (6), as shown at the bottom of the next page.

For $j = 1, 2$, the marginal distribution and density functions are given by

$$\Psi_j(y_j) = \sum_{k=1}^{K} \pi_k \Phi(y_j; \mu_{kj}, \sigma_{kj}^2),$$

$$\psi_j(y_j) = \sum_{k=1}^{K} \pi_k \phi(y_j; \mu_{kj}, \sigma_{kj}^2),$$

where $\Phi(y; \mu, \sigma^2)$ and $\phi(y; \mu, \sigma^2)$ denote the cumulative distribution function (cdf) and probability density function (pdf) of the Gaussian distribution $\mathcal{N}(\mu, \sigma^2)$, respectively.

$$f_{1,\ldots,d}(x_1, \ldots, x_d) = \prod_{i=1}^{d} f_i(x_i) \times \prod_{(a_e,b_e;S_e)\in\mathcal{E}(\mathcal{V})} c_{a_e,b_e;S_e}\left(F_{a_e|S_e}\left(x_{a_e}|x_j, j \in S_e\right), F_{b_e|S_e}\left(x_{b_e}|x_j, j \in S_e\right)\right) \tag{3}$$

Since each Ψ_j is continuous, the transformed variables $U_j = \Psi_j(Y_j)$ are uniformly distributed on (0, 1) by the probability integral transform. Hence, (U_1, U_2) admits a copula representation via Sklar's theorem. Let $\Phi(y_1, y_2; \boldsymbol{\mu}, \boldsymbol{\Sigma})$ be the cdf of bivariate Gaussian $\mathcal{N}(\boldsymbol{\mu}, \boldsymbol{\Sigma})$. With this notation, we have the cdf of (Y_1, Y_2) as $F(y_1, y_2) = \sum_{k=1}^{K} \pi_k \Phi(y_1, y_2; \boldsymbol{\mu}_k, \boldsymbol{\Sigma}_k)$. Then the GMCM copula $C(u_1, u_2)$ is given by

$$\begin{aligned} C(u_1, u_2) &= P(U_1 \le u_1, U_2 \le u_2) \\ &= P\big(Y_1 \le \Psi_1^{-1}(u_1), Y_2 \le \Psi_2^{-1}(u_2)\big) \\ &= \sum_{k=1}^{K} \pi_k \Phi\big(\Psi_1^{-1}(u_1), \Psi_2^{-1}(u_2); \boldsymbol{\mu}_k, \boldsymbol{\Sigma}_k\big). \end{aligned} \tag{7}$$

Taking derivatives yields the copula density:

$$\begin{aligned} c(u_1, u_2) &= \frac{\partial^2}{\partial u_1 \partial u_2} C(u_1, u_2) \\ &= \sum_{k=1}^{K} \pi_k \phi\big(\Psi_1^{-1}(u_1), \Psi_2^{-1}(u_2); \boldsymbol{\mu}_k, \boldsymbol{\Sigma}_k\big) \\ &\quad \times \frac{\partial}{\partial u_1} \Psi_1^{-1}(u_1) \frac{\partial}{\partial u_2} \Psi_2^{-1}(u_2) \\ &= \frac{\sum_{k=1}^{K} \pi_k \phi\big(\Psi_1^{-1}(u_1), \Psi_2^{-1}(u_2); \boldsymbol{\mu}_k, \boldsymbol{\Sigma}_k\big)}{\psi_1(\Psi_1^{-1}(u_1)) \psi_2(\Psi_2^{-1}(u_2))}. \end{aligned} \tag{8}$$

From (7), the conditional distribution of $U_1 \mid U_2 = u_2$ can be obtained using (2). Note that, for $(X_1, X_2) \sim \mathcal{N}(\boldsymbol{\mu}, \boldsymbol{\Sigma})$ with $\boldsymbol{\mu} = [\mu_1, \mu_2]^\top$ and $\boldsymbol{\Sigma} = \begin{bmatrix} \sigma_1^2 & \rho\sigma_1\sigma_2 \\ \rho\sigma_1\sigma_2 & \sigma_2^2 \end{bmatrix}$, the conditional distribution $X_1 \mid X_2 = x_2$ follows $\mathcal{N}\left(\mu_1 + \rho\frac{\sigma_1}{\sigma_2}(x_2 - \mu_2), \sigma_1^2(1-\rho^2)\right)$ and its derivative with respect to x_2 is given by (9), as shown at the bottom of the page.

Using (2) together with (9), we obtain the expression for the conditional distribution $C(u_1|u_2)$ in (10), as shown at the bottom of the page.

In [21], it is addressed that the GMCM suffers from unidentifiable parameter configurations. Since copulas are invariant to translation and scaling, only relative distances can be inferred. A partial solution suggested in [21] is anchoring the first component to have a mean of $\boldsymbol{\mu}_1 = [0, 0]^\top$ and a unit variance in each dimension, i.e., $\sigma_{11}^2 = \sigma_{12}^2 = 1$. Following [22], we additionally enforce $\rho_1 = 0$. Under this anchored specification, the GMCM takes the form

$$f(y_1, y_2) = \pi_1 \phi(y_1, y_2; \mathbf{0}, \mathbf{I}_2) + \sum_{k=2}^{K} \pi_k \phi(y_1, y_2; \boldsymbol{\mu}_k, \boldsymbol{\Sigma}_k), \tag{11}$$

where $\mathbf{I}_2$ is the 2×2 identity matrix. This model has the advantage of being able to represent the case where two random variables are independent when the number of components is 1 ($K = 1$). With this specification, the marginal cdfs and pdfs simplify to

$$\Psi_j(y_j) = \pi_1 \Phi(y_j) + \sum_{k=2}^{K} \pi_k \Phi(y_j; \mu_{kj}, \sigma_{kj}^2) \tag{12}$$

and

$$\psi_j(y_j) = \pi_1 \phi(y_j) + \sum_{k=2}^{K} \pi_k \phi(y_j; \mu_{kj}, \sigma_{kj}^2), \tag{13}$$

where $\Phi(\cdot)$ and $\phi(\cdot)$ denote the standard normal cdf and pdf, respectively.

$$\begin{aligned} &C_{a_e|S_e \cup \{b_e\}}\left(F_{a_e}\left(x_{a_e}\right) | F_{b_e}\left(x_{b_e}\right), F_i\left(x_i\right), i \in S_e\right) \\ &\quad = C_{a_e|b_e;S_e}\Big(C_{a_e|S_e}\left(F_{a_e}\left(x_{a_e}\right) | F_i\left(x_i\right), i \in S_e\right) \Big| C_{b_e|S_e}\left(F_{b_e}\left(x_{b_e}\right) | F_i\left(x_i\right), i \in S_e\right)\Big) \end{aligned} \tag{5}$$

$$\phi(y_1, y_2; \boldsymbol{\mu}_k, \boldsymbol{\Sigma}_k) = \frac{1}{2\pi\sigma_{k1}\sigma_{k2}\sqrt{1-\rho_k^2}} \exp\left(-\frac{1}{2(1-\rho_k^2)}\left\{\left(\frac{y_1-\mu_{k1}}{\sigma_{k1}}\right)^2 - 2\rho_k \frac{y_1-\mu_{k1}}{\sigma_{k1}}\frac{y_2-\mu_{k2}}{\sigma_{k2}} + \left(\frac{y_2-\mu_{k2}}{\sigma_{k2}}\right)^2\right\}\right) \tag{6}$$

$$\frac{\partial}{\partial x_2}\Phi(x_1, x_2; \boldsymbol{\mu}, \boldsymbol{\Sigma}) = \phi(x_2; \mu_2, \sigma_2^2)\Phi\left(x_1; \mu_1 + \rho\frac{\sigma_1}{\sigma_2}(x_2 - \mu_2), \sigma_1^2(1-\rho^2)\right) \tag{9}$$

$$\begin{aligned} C(u_1|u_2) &= \frac{\partial}{\partial u_2} C(u_1, u_2) = \sum_{k=1}^{K} \pi_k \frac{\partial}{\partial u_2} \Phi\big(\Psi_1^{-1}(u_1), \Psi_2^{-1}(u_2); \boldsymbol{\mu}_k, \boldsymbol{\Sigma}_k\big) \\ &= \sum_{k=1}^{K} \pi_k \frac{\partial}{\partial y_2} \Phi\big(\Psi_1^{-1}(u_1), y_2; \boldsymbol{\mu}_k, \boldsymbol{\Sigma}_k\big)\big|_{y_2 = \Psi_2^{-1}(u_2)} \frac{\partial}{\partial u_2} \Psi_2^{-1}(u_2) \\ &= \frac{\sum_{k=1}^{K} \pi_k \phi\left(\Psi_2^{-1}(u_2); \mu_{k2}, \sigma_{k2}^2\right) \Phi\left(\Psi_1^{-1}(u_1); \mu_{k1} + \rho_k \frac{\sigma_{k1}}{\sigma_{k2}}(\Psi_2^{-1}(u_2) - \mu_{k2}), \sigma_{k1}^2(1-\rho_k^2)\right)}{\psi_2(\Psi_2^{-1}(u_2))} \end{aligned} \tag{10}$$

IV. VINE LEARNING

In this section, we describe a procedure for estimating the distribution of multivariate data using the R-vine copula model introduced in Section II. Let $\mathbf{X} = \{x_{ij}\}_{1\le i\le n,,1\le j\le d}$ denote a matrix of n observations from a d-dimensional random vector. Estimating the distribution underlying $\mathbf{X}$ via the R-vine copula framework requires the specification of a triplet $(\mathcal{F}, \mathcal{V}, \mathcal{B})$ representing the marginals, the vine structure, and the associated pairwise copulas, respectively.

A. ESTIMATION OF MARGINAL DISTRIBUTIONS

We begin by estimating the marginal distributions $\mathcal{F}$, the first component of the R-vine triplet. In this work, we employ GMMs for this purpose. Since the RB utilization data take values in the unit interval, the Gaussian density, defined on the entire real line, is not directly suitable for modeling such data. To address this issue, we apply the probit transformation technique introduced in [23]. For a random variable X supported on $(0, 1)$, define $W = \Phi^{-1}(X)$. Then W is supported on $\mathbb{R}$, and its density f_W is related to that of X through $f_W(w) = f_X(\Phi(w))\phi(w)$. Given an estimate $\hat{f}_W$ of f_W, the corresponding estimate of f_X is obtained via $\hat{f}_X(x) = \hat{f}_W(\Phi^{-1}(x))/\phi(\Phi^{-1}(x))$.

For each variable X_j, $j = 1, \ldots, d$, we first transform the observations $\{x_{ij}\}_{1=1}^{n}$ into $\{w_{ij}\}_{1=1}^{n}$, where $w_{ij} = \Phi^{-1}(x_{ij})$. We then fit a GMM to the transformed data using the Expectation-Maximization (EM) algorithm [24]. If the estimated density for W_j is $\sum_{k=1}^{K} \pi_k \phi(w; \mu_k, \sigma_k^2)$, the corresponding estimate density for X_j becomes

$$f_{X_j}(x) = \frac{\sum_{k=1}^{K} \pi_k \phi\left(\Phi^{-1}(x); \mu_k, \sigma_k^2\right)}{\phi(\Phi^{-1}(x))}.$$

The number of mixture components K is selected using Cross-Validation (CV). During CV, we use the following likelihood as a metric to evaluate the fit of the model:

$$\sum_{i=1}^{n}\left\{\log\left(\sum_{k=1}^{K}\pi_k\phi\left(\Phi^{-1}(x_{ij}); \mu_k, \sigma_k^2\right)\right) - \log\phi\left(\Phi^{-1}(x_{ij})\right)\right\}.$$

B. VINE ENUMERATION

As shown in [11], the total number of distinct R-vines on d variables is $\frac{d!}{2} \times 2^{\binom{d-2}{2}}$, which grows extremely rapidly with dimension. In our application, we model RB utilization across at most six frequency bands, which represents a modest dimensionality consistent with current mobile network configurations. This dimensionality is expected to remain limited as spectrum consolidation continues. This low-dimensional setting enables a practical exhaustive search over all admissible R-vine structures to identify an appropriate model.

To facilitate this search, we first enumerate all edges that may appear in a valid R-vine. Prior approaches, such as [12] and [14], construct a graph of admissible edges at each vine level by enforcing the proximity condition, and then identify a spanning tree over this restricted graph. In contrast, we develop a direct enumeration method that leverages the structural properties of R-vines themselves. By formulating the enumeration in terms of explicit edge comparisons, our approach avoids repeatedly solving spanning-tree problems while ensuring that all admissible vine structures are systematically explored.

TABLE 1. Edge enumeration algorithm.

Input: Nodes $\{1, \ldots, d\}$ with $d \ge 3$
Output: Edge sets $\{\mathcal{G}_1, \ldots, \mathcal{G}_{d-1}\}$
$\mathcal{G}_1 \leftarrow \emptyset$
for $j = 1$ to $d - 1$ **do**
  for $l = j + 1$ to d **do**
    $\mathcal{G}_1 \leftarrow \mathcal{G}_1 \cup \{\{j, l\}\}$
  end for
end for
for $k = 2$ to $d - 1$ **do**
  $\mathcal{G}_k \leftarrow \emptyset$, $\mathcal{PG} \leftarrow \mathcal{G}_{k-1}$
  for $a \in \mathcal{G}_{k-1}$ **do**
    $\mathcal{PG} \leftarrow \mathcal{PG} \setminus \{a\}$
    if $|\mathcal{PG}| > 0$ **then**
      for $b \in \mathcal{PG}$ **do**
        if $|a \cap b| = 1$ and $|U_a \cap U_b| = k - 1$ **then**
          $\mathcal{G}_k \leftarrow \mathcal{G}_k \cup \{\{a, b\}\}$
        end if
      end for
    end if
  end for
end for
return $\{\mathcal{G}_1, \ldots, \mathcal{G}_{d-1}\}$

TABLE 2. Relative runtime comparison between the proposed enumeration method and a spanning-tree-based baseline.

Dimension d	4	5	6
Runtime ratio (Baseline / Proposed)	1.3908	1.4198	1.2529

The enumeration algorithm is provided in Table 1. For a given dimension d, it generates the collection of edge sets $\mathcal{G}_1, \ldots, \mathcal{G}_{d-1}$, where $\mathcal{G}_k$ denotes all valid edges that may appear at the k-th level tree $\mathcal{T}_k$. Each edge in the final set $\mathcal{G}_{d-1}$ corresponds to a complete R-vine structure spanning all d variables. The correctness of the algorithm is guaranteed by the following proposition.

Proposition 2: For the last set $\mathcal{G}_{d-1}$ in the algorithm of Table 1,

$$|\mathcal{G}_{d-1}| = \frac{d!}{2} \times 2^{\binom{d-2}{2}}.$$

Thus, $\mathcal{G}_{d-1}$ consists of exactly all possible R-vine structures.

Proof: See Appendix A. ■

Table 2 reports the relative runtime comparison between the proposed enumeration method and a spanning-tree-based baseline. The evaluation is conducted for dimensions up to $d = 6$, which correspond to the multiband scenarios considered in this study. For each dimension, the runtime of each method is measured over 10 independent executions and averaged, and the reported ratio is computed based on these average runtimes.

The results in Table 2 indicate that the proposed enumeration method consistently achieves lower runtime than the spanning-tree-based baseline for all considered

dimensions. Across $d = 4, 5, 6$, the proposed approach reduces the average computation time by approximately 25–40%. This efficiency can be attributed to directly enforcing the proximity condition during edge construction, which helps avoid repeated spanning-tree generation. Accordingly, in realistic multiband analyses, the proposed enumeration method may represent an attractive option for exhaustive R-vine structure exploration.

C. GMCM PARAMETER LEARNING

We now describe the procedure for estimating the parameters of the GMCM introduced in Section III, given a sample $(u_{i1}, u_{i2})_{i=1}^n$ from a pair of random variables with uniform marginals on (0, 1). The estimation is performed via maximum likelihood. From (8) and (11)-(13), the log-likelihood function for the GMCM parameters is given by

$$\begin{aligned}\mathcal{L} &= \sum_{i=1}^{n} \log c(u_{i1}, u_{i2}) \\ &= \sum_{i=1}^{n} \log f\left(\Psi_1^{-1}(u_{i1}), \Psi_2^{-1}(u_{i2})\right) \\ &\quad - \sum_{i=1}^{n} \log \psi_1\left(\Psi_1^{-1}(u_{i1})\right) - \sum_{i=1}^{n} \log \psi_2\left(\Psi_2^{-1}(u_{i2})\right).\end{aligned}$$

As noted in [17] and [21], maximizing $\mathcal{L}$ is challenging due to the non-convexity of the likelihood and the absence of closed-form expressions for the inverse marginal cdfs Ψ_j^{-1}. Consequently, the EM algorithm commonly used for GMMs cannot be applied in this setting. Instead, we employ a gradient-based likelihood optimization approach.

To compute the gradients, we must evaluate the inverse marginal cdfs $\Psi_j^{-1}(u_{ij})$ for $i = 1, \ldots, n$ and $j = 1, 2$. Since closed-form expressions for Ψ_j^{-1} are not available, we numerically approximate these values using linear interpolation of the function evaluations of Ψ_j, following the approach of [25]. Given the numerically obtained inverse cdf values, their derivatives with respect to the model parameters can be derived using the following result.

Proposition 3: Let $g(y; \theta)$ be a parametric function satisfying:

1) for each θ, the inverse $g^{-1}(u; \theta)$ with respect to y exists, and
2) g is differentiable in both y and θ.

Then the derivative of the inverse function with respect to θ is given by

$$\frac{\partial}{\partial \theta} g^{-1}(u; \theta) = -\frac{\frac{\partial}{\partial \theta} g(y; \theta)\Big|_{y=g^{-1}(u;\theta)}}{\frac{\partial}{\partial y} g(y; \theta)\Big|_{y=g^{-1}(u;\theta)}}$$

Proof: See Appendix B. ∎

Proposition 3 enables us to obtain analytic gradients of the inverse marginal cdfs from the derivatives of the corresponding cdfs. Let $y_{ij} = \Psi_j^{-1}(u_{ij})$. Using the identities

$$\begin{aligned}\frac{\partial}{\partial \mu}\Phi(x; \mu, \sigma^2) &= -\phi(x; \mu, \sigma^2), \\ \frac{\partial}{\partial \sigma}\Phi(x; \mu, \sigma^2) &= -\frac{x-\mu}{\sigma}\phi(x; \mu, \sigma^2),\end{aligned}$$

we derive

$$\begin{aligned}\frac{\partial y_{ij}}{\partial \mu_{kj}} &= \frac{\pi_k \phi(y_{ij}; \mu_{kj}, \sigma_{kj}^2)}{\psi_j(y_{ij})}, \\ \frac{\partial y_{ij}}{\partial \sigma_{kj}} &= \frac{\pi_k (y_{ij} - \mu_{kj}) \phi(y_{ij}; \mu_{kj}, \sigma_{kj}^2)}{\sigma_{kj} \psi_j(y_{ij})},\end{aligned}$$

for $k = 2, \ldots, K$. For the mixture weights, we similarly obtain

$$\begin{aligned}\frac{\partial y_{ij}}{\partial \pi_1} &= -\frac{\Phi(y_{ij})}{\psi_j(y_{ij})}, \\ \frac{\partial y_{ij}}{\partial \pi_k} &= -\frac{\Phi(y_{ij}; \mu_{kj}, \sigma_{kj}^2)}{\psi_j(y_{ij})}, \quad k = 2, \ldots, K.\end{aligned}$$

To enforce the constraints $\sigma_{kj} > 0$ and $-1 \le \rho_k \le 1$ for the covariance matrix $\boldsymbol{\Sigma}_k$, we adopt the following Cholesky-like decomposition:

$$\begin{aligned}\boldsymbol{\Sigma}_k = \boldsymbol{V}_k \boldsymbol{V}_k^\top &= \begin{bmatrix} v_{k1} & 0 \\ v_{k2} & v_{k3} \end{bmatrix} \begin{bmatrix} v_{k1} & v_{k2} \\ 0 & v_{k3} \end{bmatrix} \\ &= \begin{bmatrix} v_{k1}^2 & v_{k1}v_{k2} \\ v_{k1}v_{k2} & v_{k2}^2 + v_{k3}^2 \end{bmatrix},\end{aligned}$$

where $\boldsymbol{V}_k$ is lower triangular. This representation satisfies the required constraints for all real-valued v_{k1}, v_{k2}, and v_{k3}.

To satisfy the constraint $\sum_{k=1}^K \pi_k = 1$ with non-negative mixture weights, we reparameterize them using the softmax function:

$$\pi_k = \frac{\exp(\alpha_k)}{\sum_{k'=1}^K \exp(\alpha_{k'})}, \tag{14}$$

where each $\alpha_k \in \mathbb{R}$.

The parameter estimation thus involves computing the gradient of $\mathcal{L}$ with respect to the unconstrained variables $\{\mu_{kj}\}_{2\le k\le K, j=1,2}$, $\{v_{kj}\}_{2\le k\le K, j=1,2,3}$, and $\{\alpha_k\}_{k=1}^K$. The full derivations of the gradients are provided in Appendix C. The number of components K is selected via CV.

D. R-VINE SELECTION

We now describe how to select the optimal R-vine copula structure for a given dataset, assuming that the marginal distributions $\mathcal{F}$ have been estimated as discussed in Section IV-A. The goal is to determine the remaining components of the triplet, namely the vine structure $\mathcal{V}$ and the set of bivariate copulas $\mathcal{B}$, by maximizing the likelihood over all admissible R-vine configurations. Since copulas operate on uniform margins, we first transform the original data $\{x_{ij}\}_{1\le i\le n, 1\le j\le d}$ into $\{u_{ij} = F_j(x_{ij})\}_{1\le i\le n, 1\le j\le d}$, which are uniformly distributed on (0, 1). The subsequent vine construction and parameter estimation are then performed using this transformed data. Based on (3) and (4), the

log-likelihood of the transformed data under a given vine structure $(\mathcal{V}, \mathcal{B})$ is given by

$$\sum_{i=1}^{n} \sum_{\substack{(a,b;S) \\ \in \mathcal{E}(\mathcal{V})}} \log c_{a,b;S}\Big(C_{a|S}\left(u_{ia}|u_{ij}, j \in S\right), C_{b|S}\left(u_{ib}|u_{ij}, j \in S\right)\Big). \tag{15}$$

As mentioned in Section IV-B, we choose the one that maximizes the value of (15) for all possible vine structures. To this end, it is necessary to learn GMCM parameters for all possible edges that can be enumerated through the algorithm in Table 1. In this work, we sequentially apply GMCM parameter learning to the sets of edges $\{\mathcal{G}_1, \ldots, \mathcal{G}_{d-1}\}$ generated by the algorithm. As can be seen in (15), the copula for an edge belonging to $\mathcal{G}_k$ for $k \geq 2$ is determined by fitting the conditional copula values for the two edges belonging to $\mathcal{G}_{k-1}$ that compose it. According to the third of Proposition 1, the conditional copula that can be used in the next higher-order tree for an edge $(a, b; S)$ is $C_{a|b;S}$ or $C_{b|a;S}$, so calculation of these is also required after establishing the copula $C_{a,b;S}$. The specific process of establishing copulas for all possible edges is described in Table 3.

Once the collection $\{C_{a,b;S}\}_{(a,b;S)\in\mathcal{E}(\mathcal{V})}$ is obtained for all candidate edges, we evaluate the complete log-likelihood for each R-vine structure. Since each element of $\mathcal{G}_{d-1}$ corresponds to a valid full R-vine, we traverse backward through the hierarchy of trees to accumulate the likelihood contributions. This backtracking process is formalized in Table 4.

Then we select the structure in $\mathcal{G}_{d-1}$ that yields the highest log-likelihood under (15), and assign the corresponding structure and associated GMCMs to $\mathcal{V}$ and $\mathcal{B}$, respectively.

V. EMPIRICAL VALIDATION ON RB UTILIZATION DATA

In this section, we apply the proposed density estimation methodology to RB utilization data collected from the control channel signals of LTE BSs operating at a site where a Mobile Network Operator (MNO) deploys multiple frequency bands.

A. DATA DESCRIPTION

The dataset used in this study was collected using the ALTETRI platform (Analyzer of LTE Traffic and Radio Information) [4], which extracts scheduling information by decoding all downlink control information transmitted from an LTE BS. To capture multiband scheduling behavior, simultaneous measurements were conducted across multiple LTE bands at a single site using multiple ALTETRI units. The measurement site was located in a high-traffic area operated by one of Korea's major mobile network operators, which utilizes five LTE bands. Data was collected near Gangnam Station in Seoul, South Korea–an area known for heavy mobile traffic–over 8 to 10 hours on weekdays during the following months: June 2021, August 2021, and April, May, July, August, and November 2022. The site was selected to enable reliable simultaneous observation across all deployed frequency bands and to capture multiband spectrum utilization under traffic-intensive conditions relevant to conservative spectrum planning and refarming.

Each data point is a five-dimensional vector representing the average percentage of RBs scheduled per second in each of the five bands. Since LTE scheduling operates at a granularity of 1 ms (i.e., per subframe), each data point summarizes the outcome of 1,000 scheduling decisions.

TABLE 3. GMCM fitting for all possible edges.

Input: Data $\{u_{ij}\}_{1\leq i\leq n, 1\leq j\leq d}$, enumerated edges $\{\mathcal{G}_k\}_{k=1}^{d-1}$
Output: GMCMs $C_{a,b;S}$ for $(a,b;S) \in \cup_{k=1}^{d-1}\mathcal{G}_k$

for $e = (a_e, b_e) \in \mathcal{G}_1$ **do**
  find a GMCM C_{a_e,b_e} that fits the data $\{(u_{i,a_e}, u_{i,b_e})\}_{i=1}^n$
  $\mathbf{v}_e \leftarrow \{C_{a_e|b_e}(u_{i,a_e}|u_{i,b_e})\}_{i=1}^n$, $\mathbf{v}'_e \leftarrow \{C_{b_e|a_e}(u_{i,b_e}|u_{i,a_e})\}_{i=1}^n$
  (These are calculated by (10))
end for
for $k = 2$ to $d-1$ **do**
  for $e = (a_e, b_e; S_e) = (a_e, b_e; s_{e,1}, \ldots, s_{e,k-1}) \in \mathcal{G}_k$ **do**
    for the two edges in $\mathcal{G}_{k-1}$ that form e **do**
      $e \leftarrow \{e_1, e_2\}$ so that,
      with $e_l = (a_{e_l}, b_{e_l}; s_{e_l,1}, \ldots, s_{e_l,k-2})$ for $l = 1, 2$,
      $U_{e_1} = \{a_e, s_{e,1}, \ldots, s_{e,k-1}\}$ and $U_{e_2} = \{b_e, s_{e,1}, \ldots, s_{e,k-1}\}$
      if $a_e = a_{e_1}$ **then**
        $\mathbf{w}_1 \leftarrow \mathbf{v}_{e_1}$
      else
        $\mathbf{w}_1 \leftarrow \mathbf{v}'_{e_1}$
      end if
      if $b_e = a_{e_2}$ **then**
        $\mathbf{w}_2 \leftarrow \mathbf{v}_{e_2}$
      else
        $\mathbf{w}_2 \leftarrow \mathbf{v}'_{e_2}$
      end if
      find a GMCM $C_{a_e,b_e;S_e}$ that fits the data $\{\mathbf{w}_1, \mathbf{w}_2\}$
      if $k < d-1$, with $\mathbf{w}_l = \{w_{il}\}_{i=1}^n$ for $l = 1, 2$ **then**
        $\mathbf{v}_e \leftarrow \{C_{a_e|\{b_e\}\cup S_e}(u_{i,a_e}|u_{i,b_e}, u_{i,j}, j \in S_e)\}_{i=1}^n$
          $= \{C_{a_e|b_e;S_e}(w_{i1}|w_{i2})\}_{i=1}^n$,
        $\mathbf{v}'_e \leftarrow \{C_{b_e|\{a_e\}\cup S_e}(u_{i,b_e}|u_{i,a_e}, u_{i,j}, j \in S_e)\}_{i=1}^n$
          $= \{C_{b_e|a_e;S_e}(w_{i2}|w_{i1})\}_{i=1}^n$
      end if
    end for
  end for
end for
return $\{C_e\}_{e\in\cup_{k=1}^{d-1}\mathcal{G}_k}, \{\mathbf{v}_e, \mathbf{v}'_e\}_{e\in\cup_{k=1}^{d-2}\mathcal{G}_k}$

TABLE 4. Calculation of the log-likelihood for an R-vine structure.

Input: Data $\{u_{ij}\}_{1\leq i\leq n, 1\leq j\leq d}$, an edge $e \in \mathcal{G}_{d-1}$,
  copulas and their densities $\{C_{\tilde{e}}, c_{\tilde{e}}\}_{\tilde{e}\in\cup_{k=1}^{d-1}\mathcal{G}_k}$,
  vectors of conditional copula values $\{\mathbf{v}_{\tilde{e}}, \mathbf{v}'_{\tilde{e}}\}_{\tilde{e}\in\cup_{k=1}^{d-2}\mathcal{G}_k}$
Output: Log-likelihood for the R-vine structure associated with e

For e, $\mathbf{w}_1 \leftarrow \{w_{i1}\}_{i=1}^n$, $\mathbf{w}_2 \leftarrow \{w_{i2}\}_{i=1}^n$ (as in Table 3)
loglik $\leftarrow \sum_{i=1}^n \log c_e(w_{i1}, w_{i2})$
$\mathcal{CH} \leftarrow \{e_1, e_2\}$ where $e = \{e_1, e_2\}$ with $e_1, e_2 \in \mathcal{G}_{d-2}$
for $k = d-2$ to 1 **do**
  $\mathcal{TCH} \leftarrow \emptyset$
  for $\tilde{e} \in \mathcal{CH}$ **do**
    $\mathbf{w}_1 \leftarrow \{w_{i1}\}_{i=1}^n$, $\mathbf{w}_2 \leftarrow \{w_{i2}\}_{i=1}^n$ (as in Table 3)
    loglik $\leftarrow$ loglik $+ \sum_{i=1}^n \log c_{\tilde{e}}(w_{i1}, w_{i2})$
    $\mathcal{TCH} \leftarrow \mathcal{TCH} \cup \{\tilde{e}_1, \tilde{e}_2\}$ where $\tilde{e} = \{\tilde{e}_1, \tilde{e}_2\}$ with $\tilde{e}_1, \tilde{e}_2 \in \mathcal{G}_{k-1}$
  end for
  $\mathcal{CH} \leftarrow \mathcal{TCH}$
end for
return loglik

TABLE 5. KS test results for marginal distributions.

Band No.	1	2	3	4	5
p-value	0.3495	0.9265	0.4423	0.1198	0.7117

To reduce temporal dependence and approximate independent and identically distributed behavior, data points were sampled at regular intervals using the decorrelation method proposed in [26].

A total of 751 data points were obtained and are denoted by $\{x_{ij}\}_{1\le i\le 751, 1\le j\le 5}$, where i indexes time and j indexes frequency bands. Among these, 561 samples were used for training and 190 for testing. During the training phase, threefold CV was performed by partitioning the training set into three subsets of equal size.

B. DENSITY ESTIMATION RESULTS

1) MARGINAL DISTRIBUTION ESTIMATION

We begin by presenting the results of the marginal distribution estimation for RB utilization across the five frequency bands, following the methodology described in Section IV-A. For each band, a GMM is fitted to the transformed training samples using the EM algorithm. The number of mixture components is selected via CV, after which the model is retrained using the full training dataset.

To evaluate the quality of the marginal fit, we apply the Kolmogorov–Smirnov (KS) test to the held-out test set. The results, summarized in Table 5, indicate that for all five bands, the null hypothesis that the test samples are drawn from the estimated distribution cannot be rejected at the 10% significance level.

TABLE 6. Selected vine structure $\mathcal{V}$.

Tree	Edges
$\mathcal{T}_1$	$(1,4),(2,5),(3,4),(3,5)$
$\mathcal{T}_2$	$(1,3;4),(2,3;5),(4,5;3)$
$\mathcal{T}_3$	$(1,5;3,4),(2,4;3,5)$
$\mathcal{T}_4$	$(1,2;3,4,5)$

2) JOINT DISTRIBUTION ESTIMATION AND EVALUATION

We now present the results of fitting the joint distribution of multiband RB utilization using the proposed R-vine copula model. Let F_j denote the marginal distribution for band j, obtained as described in Section V-B1, for $j = 1,\ldots,5$. Following the procedure in Section IV-D, the original observations $\{x_{ij}\}$ are transformed into uniform scores $u_{ij} = F_j(x_{ij})$, and the vine learning algorithm is applied to the resulting uniform data.

For each edge appearing in the candidate vine structures generated by the enumeration algorithm in Table 1, a GMCM is fitted to the corresponding bivariate or conditional data. When fitting the GMCMs as described in Table 3, the number of mixture components is selected using CV, consistent with the approach used for the marginal distributions. After selecting the number of components, the GMCM parameters are estimated using the full training dataset. The ADAM [27] optimizer is applied for gradient ascent to adapt the GMCM parameters. The final vine structure $\mathcal{V}$ is chosen as the one achieving the highest sum of CV scores across all edges that constitute the structure. The selected R-vine structure is reported in Table 6.

TABLE 7. The per-sample average log-likelihood of the test data for each density estimation method.

GMM	BMM	Tree-by-tree	Proposed	GGM	NSF
1.756	1.86	2.173	2.293	1.418	−0.037

TABLE 8. Fasano-Franceschini test results for multivariate distributions of all band combinations.

Bands	p-value	Bands	p-value	Bands	p-value
$1,2$	0.2209	$1,2,3$	0.1173	$1,2,3,4$	0.1395
$1,3$	0.3356	$1,2,4$	0.3452	$1,2,3,5$	0.2726
$1,4$	0.6044	$1,2,5$	0.2122	$1,2,4,5$	0.4313
$1,5$	0.2155	$1,3,4$	0.4849	$1,3,4,5$	0.371
$2,3$	0.4144	$1,3,5$	0.3815	$2,3,4,5$	0.4391
$2,4$	0.6855	$1,4,5$	0.5737	$1,2,3,4,5$	0.2303
$2,5$	0.7969	$2,3,4$	0.4875		
$3,4$	0.6644	$2,3,5$	0.6069		
$3,5$	0.693	$2,4,5$	0.8715		
$4,5$	0.7663	$3,4,5$	0.4127		

We evaluate the performance of the proposed vine copula model by computing the log-likelihood on the held-out test data. For comparison, we include two mixture-based alternatives: a GMM and the Beta mixture model (BMM) of [28], which is designed for variables with bounded support such as RB utilization. For all methods, the number of mixture components is selected via CV, and parameter estimation is carried out using the full training dataset. For vine-based approaches, we also consider the tree-by-tree structure selection method of [12], which is widely used in low-dimensional settings and serves as an additional baseline. Its corresponding vine structure is learned from the training data in the same manner. In addition, we include two widely used multivariate dependency learning baselines. First, a Gaussian Graphical Model (GGM) [29] is considered to represent conditional dependencies under a Gaussian assumption. Second, we include a deep generative density estimator based on Neural Spline Flows (NSF) [30], which is a state-of-the-art likelihood-based normalizing flow model. Both the GGM and NSF baselines are applied to probit-transformed uniform scores. For both models, log-likelihoods are obtained by correcting for the Jacobian of the probit transformation. Hyperparameters for both models are selected using CV. Table 7 reports the per-sample average log-likelihood values on the test set.

As expected, the BMM outperforms the GMM due to its ability to accommodate the bounded support of RB utilization. The proposed vine copula model achieves the highest log-likelihood among all methods, benefiting from its expressive construction based on flexible bivariate components. Furthermore, even when compared to the tree-by-tree vine model, the exhaustive search approach yields superior performance, demonstrating the advantage of full structure exploration in low-dimensional settings. The GGM baseline yields a lower log-likelihood than the proposed vine copula model. Under the regularization level selected by CV, the estimated precision matrix does not exhibit pronounced sparsity, indicating that the data do not strongly support a sparse conditional independence structure under

a Gaussian assumption. As a result, GGM is less effective in capturing inter-band dependencies in this setting than the proposed vine copula framework. The NSF provides a flexible deep generative baseline, but its test log-likelihood is also lower than that of the proposed vine copula model. This difference can be attributed to the nature of the problem, where the number of jointly modeled variables is small and different frequency bands play distinct operational roles. In such settings, strong and structured inter-band interactions are expected. Explicitly modeling dependency relationships, as in copula-based approaches, can therefore be more effective than relying on highly expressive but less structured transformations.

To further evaluate the adequacy of the fitted joint distribution, we conduct goodness-of-fit tests for all combinations of bands. For each test, synthetic samples are generated from the fitted vine copula model using the sampling procedure described in [19], with the number of simulated points matched to the size of the test set. We employ the Fasano–Franceschini test [31], a multidimensional extension of the two-sample Kolmogorov–Smirnov test. The resulting p-values, reported in Table 8, indicate that at the 10% significance level, the hypothesis that the test and simulated samples originate from the same distribution cannot be rejected for any band combination. These findings suggest that the proposed model provides an accurate representation of the joint distribution of RB utilization.

TABLE 9. Spearman's rank correlation value for RB utilization of each band pair.

Bands	$1,2$	$1,3$	$1,4$	$1,5$	$2,3$
Corr.	0.3732	0.3239	0.4378	0.219	0.5031
Bands	$2,4$	$2,5$	$3,4$	$3,5$	$4,5$
Corr.	0.425	0.5302	0.4532	0.473	0.3528

Figure 2 presents scatter plots comparing the test data with simulated samples for several two-dimensional band combinations. The close visual agreement between the empirical and synthetic distributions further supports the adequacy of the proposed model.

VI. SPECTRUM UTILIZATION ANALYSIS USING THE FITTED MODEL

In this section, we analyze LTE multiband spectrum utilization using the multivariate distribution estimated in Section V. By drawing samples from the learned distribution, we can systematically examine possible usage scenarios, quantify uncertainty, and evaluate potential outcomes [32]. To this end, we generate one million five-dimensional samples of multiband RB utilization from the fitted model.

A. RB UTILIZATION PATTERNS ACROSS BAND PAIRS

We examine the joint utilization patterns of band pairs to gain insight into how different frequency bands cooperate to achieve desired communication performance. In particular, we aim to identify which bands are jointly activated to support higher throughput, as in carrier aggregation scenarios, and which bands are primarily utilized for coverage assurance.

To begin, we compute Spearman's rank correlation coefficients as scalar measures of monotonic association. Table 9 presents the correlation values for each band pair.

While the results suggest a general trend of positive correlation in RB utilization across all band pairs, such scalar summaries are insufficient for uncovering detailed dependency patterns. To gain finer insights, we employ the dependence map framework proposed by [33], which visualizes local dependence between two variables over the unit square $[0,1]^2$.

To construct dependence maps, we divide $[0,1]^2$ into a 50×50 grid, yielding 2500 cells. For each band pair, if a grid cell contains fewer than 200 of the one million simulated samples, it is marked as having insufficient data and colored black. For cells with sufficient data, the local dependence function is estimated at the cell center, and its sign is tested via permutation-based local independence tests. Each cell is assigned a value of $+1$ (positive local dependence), 0 (local independence), or -1 (negative local dependence), and is rendered in white, light gray, or gray, respectively.

The dependence maps for all band pairs are shown in Figure 3. From the maps, we observe several notable patterns:

- General pattern: Most band pairs show positive local dependence when both bands are either lightly or heavily utilized, indicating synchronized behavior under low or high load.
- Bands 1 and 2: A linear cluster of positive dependence extends up to around 70% utilization, indicating cooperative activation in moderate traffic conditions.
- Bands 1 and 5: Despite sufficient data across most regions, local dependence values remain close to zero. This implies that these bands operate independently, without strong interaction.
- Band 1 with others: Band 1 shows patches of negative local dependence in high-utilization regions when paired bands are underutilized. This may reflect its role in supporting coverage when other bands are less active.
- Bands 2 and 3 / 2 and 4: These pairs exhibit structured nonlinear dependence. For instance, the 2–4 pair forms a cubic-like pattern, where usage shifts between bands as overall traffic increases. Such patterns suggest dynamic role switching or complementary use depending on load level.
- Bands 2 and 5: Positive dependence appears in low-utilization areas, while a narrow region of negative dependence emerges when band 2 is heavily used and band 5 is lightly loaded. This suggests possible load-splitting behavior under certain conditions.
- Bands 3 and 5 / 4 and 5: These band pairs show strong linear clusters of positive dependence with slopes close to 1, indicating that they tend to be used together in roughly equal proportions. Notably, for 3–5, a small region of negative dependence emerges when band

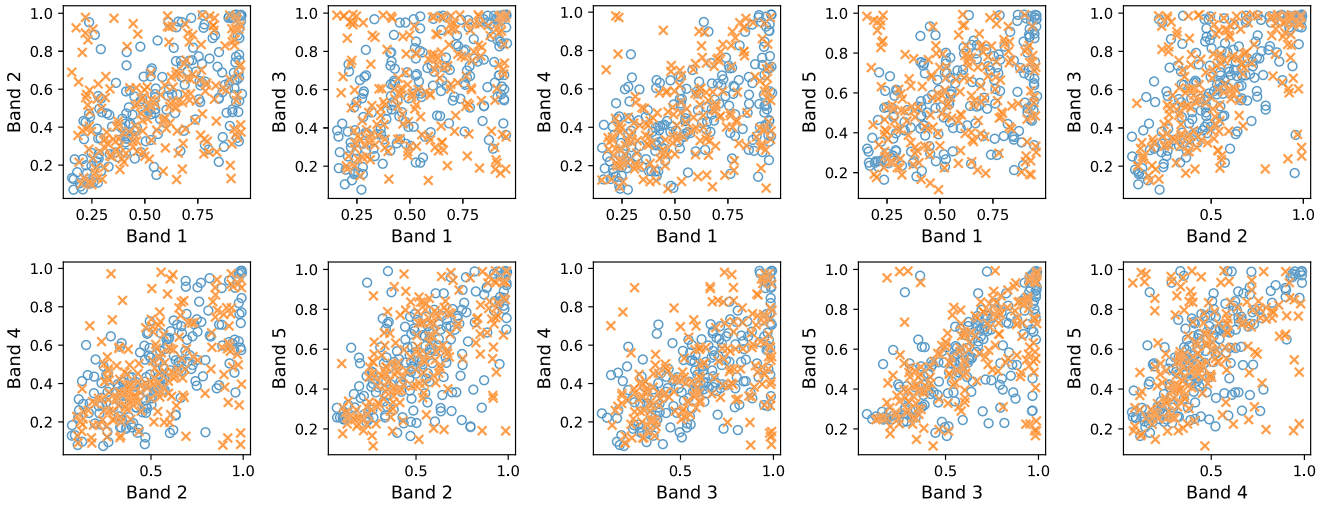

FIGURE 2. Scatter plots of test data and simulated samples for two-dimensional band combinations. Circles and crosses indicate test data and simulated samples, respectively.

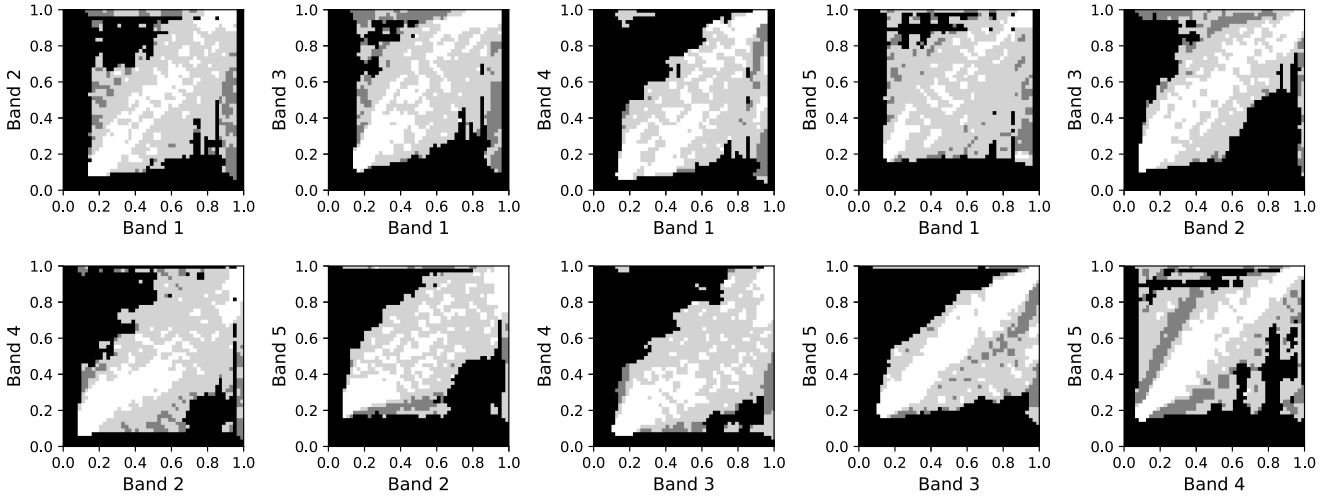

FIGURE 3. Dependency maps of RB utilization for band pairs. In the dependency map, each grid is colored white for positive local dependence, light gray for local independence, gray for negative local dependence, and black for insufficient data to consider local dependence.

3 exceeds 80% utilization, suggesting active balancing to avoid overloading.

- Bands 3 and 4: Unlike the above, this pair exhibits minimal dependence in moderate utilization regions. This absence of interaction implies that bands 3 and 4 are not typically aggregated or jointly activated under regular traffic loads.

These observations suggest that carrier aggregation patterns differ across bands, and that dynamic balancing of utilization between complementary bands is common. The dependence map offers rich insights beyond what scalar correlation can reveal, enabling interpretable diagnostics of multiband spectrum usage.

B. BAND UTILIZATION PRIORITY

Here, we examine which bands are preferentially utilized in the multiband LTE system under consideration. Let R_j denote the RB utilization of band j for $j = 1, \ldots, 5$, and let O_j denote the average RB utilizations of the remaining four bands:

$$O_j = \frac{1}{4} \sum_{k \neq j} R_k.$$

For a given threshold $\xi \in (0, 1)$, we define

$$p_j(\xi) = P(O_j > \xi | R_j > \xi),$$

which represents the probability that the other bands exceed utilization level ξ, conditioned on band j doing so. A low value of $p_j(\xi)$ suggests that band j tends to reach high utilization before the others and thus may be preferentially utilized. Figure 4 shows the values of $p_j(\xi)$ for several values of ξ. As seen in the figure, band 1 consistently exhibits the lowest values of the probability, indicating that it is likely to be utilized earlier than the others, possibly owing to its favorable propagation characteristics for coverage. In contrast, band 4 shows the highest values of the probability over most of the range, implying that it is generally utilized later and likely used to balance the traffic load among bands.

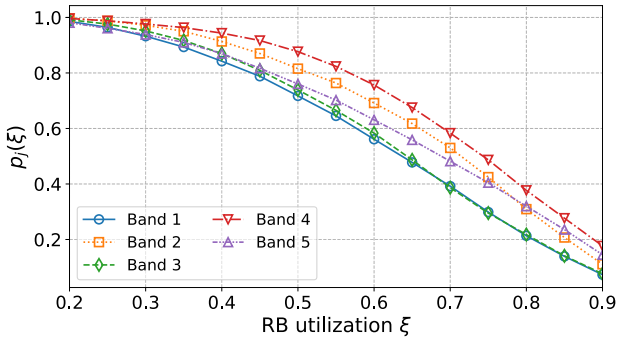

FIGURE 4. The values of $p_j(\xi) = P(O_j > \xi | R_j > \xi)$ for several ξ's for all bands.

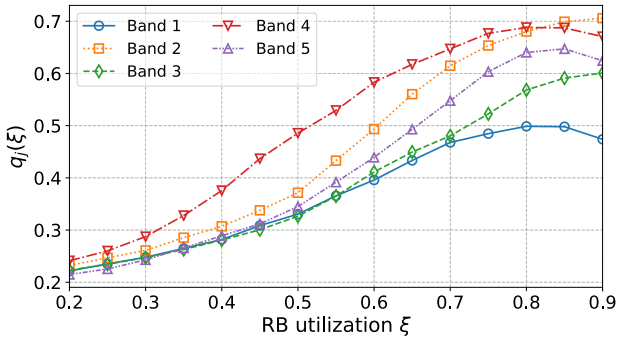

FIGURE 5. The values of $q_j(\xi) = P(R > 0.7 | R_j > \xi)$ for several ξ's for all bands.

To further investigate how individual band utilization relates to overall cell capacity, we consider a site-level utilization metric. Let

$$R = \frac{1}{5}\sum_{j=1}^{5} R_j$$

denote the average RB utilization across all five bands. Following [34], a value of $R > 0.7$ can serve as an indicator of spectrum saturation in terms of service quality, particularly regarding the support for seamless video streaming for new users. We define the conditional probability

$$q_j(\xi) = P(R > 0.7 | R_j > \xi),$$

which represents the probability that the entire cell is saturated, given that band j exceeds a threshold ξ. Figure 5 shows the values of $q_j(\xi)$ over various threshold levels. Consistent with the earlier findings, band 1 shows the lowest saturation probabilities, reinforcing its role as a coverage-first band. Band 4 exhibits the highest saturation probabilities, suggesting that its increased usage correlates with overall resource exhaustion. Interestingly, band 2 demonstrates mixed characteristics. For high thresholds ($\xi > 0.85$), the value of $p_2(\xi)$ drops sharply, while $q_2(\xi)$ becomes the highest among all bands. This suggests that band 2 can serve both as an early-utilization band (like band 1) and as a high-utilization band that signals site saturation (like band 4), highlighting its dual operational role.

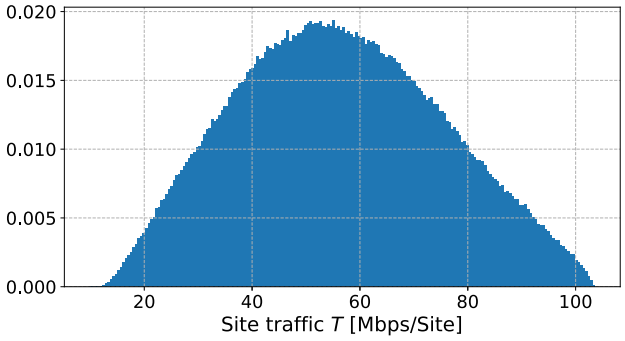

FIGURE 6. Histogram of the cell site traffic.

C. OFFERED TRAFFIC

The RB utilization of multiple bands can be used to infer the amount of traffic handled at a given cell site. As in [35], we utilize monthly data collected from MNOs in Seoul, which include busy-hour RB utilization and corresponding traffic measurements. From these measurements, band-specific spectral efficiencies can be derived. For $j = 1, \ldots, 5$, let w_j and η_j be the bandwidth (MHz) and the spectral efficiency (bps/Hz) of band j, respectively. Then, for a given multi-band RB utilization vector $(R_1, R_2, R_3, R_4, R_5)$, the traffic T processed in the cell site (in Mbps) can be computed as $T = \sum_{j=1}^{5} R_j w_j \eta_j$. In this study, the spectral efficiency values were derived from MNO-provided measurements obtained during the same months in which our RB utilization data were collected. Figure 6 presents a histogram of the resulting cell-site traffic distribution. The traffic exhibits an approximately symmetric bell-shaped pattern.

The above calculations can be incorporated into network-level simulations. In particular, the conditional probability distribution $P(R_1, \ldots, R_5 | T)$ for a specified cell-site traffic level T can be obtained from the estimated multivariate distribution of multiband RB utilization. This conditional distribution enables Monte Carlo simulation of how a cell allocates resources across multiple frequency bands in response to imposed traffic.

VII. CONCLUSION

In this work, we presented a comprehensive methodology for accurate multivariate density estimation in low-dimensional settings, with a particular focus on modeling dependencies among frequency band utilizations in mobile communication networks. Building on the R-vine copula framework, we developed an efficient algorithm that exhaustively enumerates and evaluates all admissible vine structures. This exhaustive search remains computationally feasible and practically effective when the dimensionality is moderate. To enhance modeling flexibility, we incorporated GMCMs into each pair-copula component and derived exact gradients to enable fully differentiable likelihood-based parameter learning.

The proposed framework was applied to real-world LTE multiband resource usage data. Empirical evaluations showed

that the estimated distributions fit the observed data well, as supported by goodness-of-fit testing, and that the model can provide interpretable insights into multiband spectrum utilization behavior. Beyond this application, the proposed approach offers a principled and flexible solution for learning interpretable joint distributions in low-dimensional multivariate settings. Such capabilities are particularly valuable in domains where strong dependencies exist among variables and model transparency is essential.

APPENDIX A
PROOF OF PROPOSITION 2

For convenience, we denote $\mathcal{G}_l$ when the number of elements is k as $\mathcal{G}_{k,l}$ for $1 \le l \le k-1$. Since $\mathcal{G}_{k,1}$ consists of the pairs of two elements in $\{1,\dots,k\}$, $|\mathcal{G}_{k,1}| = \binom{k}{2}$. For $k=3$, any two elements in $\mathcal{G}_{3,1}$ can make an edge. Thus, we have $|\mathcal{G}_{3,2}| = \binom{3}{2} = 3$. For the use of inductive argument, we assume that $|\mathcal{G}_{k,k-1}| = \frac{k!}{2}\times 2^{\binom{k-2}{2}}$ for $k = 3,4,\dots,d-1$. Now, we show that $|\mathcal{G}_{d,d-1}| = \frac{d!}{2}\times 2^{\binom{d-2}{2}}$. For $1 \le k \le d-2$, any element in $\mathcal{G}_{d,k}$ has a complete union of size $k+1$. For $a \in \mathcal{G}_{d,k}$, the number of elements in $\mathcal{G}_{d,k}$ that have the same complete union of a is equal to $|\mathcal{G}_{k+1,k}| = \frac{(k+1)!}{2} \times 2^{\binom{k-1}{2}}$, i.e., $|\{b \in \mathcal{G}_{d,k} | U_a = U_b\}| = |\mathcal{G}_{k+1,k}|$. Since $\{1,\dots,d\}$ has $\binom{d}{k+1}$ subsets of size $k+1$, we have

$$|\mathcal{G}_{d,k}| = \binom{d}{k+1} \times |\mathcal{G}_{k+1,k}| = \frac{1}{(d-k-1)!}\frac{d!}{2}2^{\binom{k-1}{2}}.$$

For an element $a \in \mathcal{G}_{d,d-3}$, let $\mathcal{N}_a = \{b \in \mathcal{G}_{d,d-3} | \{a,b\} \in \mathcal{G}_{d,d-2}\}$. By the symmetry, for every node $a \in \mathcal{G}_{d,d-3}$, $|\mathcal{N}_a|$ is the same. Also, an edge $\{a,b\}$ serves for counting of 1 in both $|\mathcal{N}_a|$ and $|\mathcal{N}_b|$. Thus, we have the relation

$$\frac{|\mathcal{G}_{d,d-3}| \times |\mathcal{N}_a|}{2} = |\mathcal{G}_{d,d-2}|,$$

and

$$\begin{aligned}|\mathcal{N}_a| &= 2 \times \frac{|\mathcal{G}_{d,d-2}|}{|\mathcal{G}_{d,d-3}|} \\ &= 2 \times \frac{(d-(d-3)-1)!}{(d-(d-2)-1)!}2^{\frac{(d-3)(d-4)-(d-4)(d-5)}{2}} \\ &= 2 \times 2^{d-3}.\end{aligned}$$

Since an $a \in \mathcal{G}_{d,d-3}$ has the complete union of size $d-2$, there are $c_1, c_2 \in \{1,\dots,d\}$ such that $U_a \cup \{c_1,c_2\} = \{1,\dots,d\}$. Thus, among the elements of $\mathcal{N}_a$, 2^{d-3} elements, which are the half, contain c_1 in their complete unions, and the other half contains c_2 in their complete unions. Let $\mathcal{N}_{a,1} = \{b \in \mathcal{N}_a | c_1 \in U_b\}$ and $\mathcal{N}_{a,2} = \{b \in \mathcal{N}_a | c_2 \in U_b\}$. An edge belonging to $\mathcal{G}_{d,d-1}$ that shares a has the form of $\{\{a,a_1\},\{a,a_2\}\}$ where $a_1 \in \mathcal{N}_{a,1}$ and $a_2 \in \mathcal{N}_{a,2}$. Thus, there are $2^{d-3} \times 2^{d-3} = 2^{2d-6}$ elements in $\mathcal{G}_{d,d-1}$ that shares a. Finally, we have

$$\begin{aligned}|\mathcal{G}_{d,d-1}| &= \left|\mathcal{G}_{d,d-3} \times 2^{2d-6}\right| \\ &= \frac{1}{2!}\frac{d!}{2}2^{\binom{d-4}{2}} \times 2^{2d-6} = \frac{d!}{2}2^{\frac{(d-4)(d-5)}{2}+\frac{4d-12}{2}-1} \\ &= \frac{d!}{2}2^{\frac{d^2-5d+6}{2}} = \frac{d!}{2}2^{\frac{(d-2)(d-3)}{2}} = \frac{d!}{2}2^{\binom{d-2}{2}}.\end{aligned}$$

APPENDIX B
PROOF OF PROPOSITION 3

We have

$$u = g\left(g^{-1}(u;\theta);\theta\right).$$

Differentiating the left-hand side with respect to θ gives

$$\frac{\partial u}{\partial \theta} = 0.$$

Differentiating the right-hand side with respect to θ gives

$$\begin{aligned}\frac{\partial}{\partial\theta}g\left(g^{-1}(u;\theta);\theta\right) &= \frac{\partial}{\partial y}g(y;\theta)\Big|_{y=g^{-1}(u;\theta)}\frac{\partial}{\partial\theta}g^{-1}(u;\theta) \\ &\quad + \frac{\partial}{\partial\theta}g(y;\theta)\Big|_{y=g^{-1}(u;\theta)}.\end{aligned}$$

Equating the above two equations gives the result.

APPENDIX C
GRADIENT OF LOG-LIKELIHOOD

We first derive the derivatives of $\mathcal{L}$ with respect to $\{\mu_{kj}\}_{2\le k\le K, j=1,2}$:

$$\frac{\partial}{\partial\mu_{kj}}\mathcal{L} = \sum_{i=1}^{n}\left(\frac{\partial}{\partial\mu_{kj}}\log f(y_{i1},y_{i2}) - \frac{\partial}{\partial\mu_{kj}}\log\psi_j(y_{ij})\right). \tag{16}$$

The first term of (16) expands to the expression in (17), as shown at the bottom of the page.

For the first term in the numerator of (17), we have

$$\begin{aligned}\frac{\partial}{\partial y_{ij}}\phi(y_{i1},y_{i2};\mathbf{0},\mathbf{I}_2) &= \frac{\partial}{\partial y_{ij}}\frac{1}{2\pi}\exp\left(-\frac{1}{2}(y_{i1}^2+y_{i2}^2)\right) \\ &= \phi(y_{i1},y_{i2};\mathbf{0},\mathbf{I}_2)\cdot(-y_{ij}).\end{aligned} \tag{18}$$

For the second term in the numerator of (17), we obtain the expression in (19), as shown at the bottom of the next page, where $\hat{j} \in \{1,2\}\setminus\{j\}$. The third term in the numerator of (17)

$$\begin{aligned}\frac{\partial}{\partial\mu_{kj}}\log f(y_{i1},y_{i2}) &= \frac{\frac{\partial}{\partial\mu_{kj}}\left\{\pi_1\phi(y_{i1},y_{i2};\mathbf{0},\mathbf{I}_2)+\sum_{l=2}^{K}\pi_l\phi(y_{i1},y_{i2};\boldsymbol{\mu}_l,\boldsymbol{\Sigma}_l)\right\}}{f(y_{i1},y_{i2})} \\ &= \frac{\frac{\partial y_{ij}}{\partial\mu_{kj}}\frac{\partial}{\partial y_{ij}}\left\{\pi_1\phi(y_{i1},y_{i2};\mathbf{0},\mathbf{I}_2)+\sum_{l=2}^{K}\pi_l\phi(y_{i1},y_{i2};\boldsymbol{\mu}_l,\boldsymbol{\Sigma}_l)\right\}+\pi_k\frac{\partial}{\partial\mu_{kj}}\phi(y_{i1},y_{i2};\boldsymbol{\mu}_k,\boldsymbol{\Sigma}_k)}{f(y_{i1},y_{i2})}.\end{aligned} \tag{17}$$

expands to the expression in (20), as shown at the bottom of the page.

For the second term of (16), we obtain the expression in (21), as shown at the bottom of the page. For the first and second term in the numerator of (21), we have

$$\frac{\partial}{\partial y_{ij}}\phi(y_{ij}) = \frac{\partial}{\partial y_{ij}}\frac{1}{2\sqrt{\pi}}\exp\left(-\frac{1}{2}y_{ij}^2\right) = \phi(y_{ij})(-y_{ij})$$

and

$$\frac{\partial}{\partial y_{ij}}\phi(y_{ij};\mu_{kj},\sigma_{kj}^2) = \phi(y_{ij};\mu_{kj},\sigma_{kj}^2)\left(-\frac{y_{ij}-\mu_{kj}}{\sigma_{kj}^2}\right),$$

respectively. The last term in the numerator of (21) is

$$\frac{\partial}{\partial \mu_{kj}}\phi(y_{ij};\mu_{kj},\sigma_{kj}^2) = \phi(y_{ij};\mu_{kj},\sigma_{kj}^2)\frac{y_{ij}-\mu_{kj}}{\sigma_{kj}^2}.$$

Next we derive the derivatives of $\mathcal{L}$ with respect to $\{v_{kj}\}_{2\le k\le K, j=1,2,3}$. To this end, we first derive the derivatives of $\mathcal{L}$ with respect to $\{\sigma_{kj}\}_{2\le k\le K, j=1,2}$

$$\frac{\partial}{\partial \sigma_{kj}}\mathcal{L} = \sum_{i=1}^{n}\left(\frac{\partial}{\partial \sigma_{kj}}\log f(y_{i1},y_{i2}) - \frac{\partial}{\partial \sigma_{kj}}\log\psi_j(y_{ij})\right). \quad (22)$$

The first term of (22) expands to the expression in (23), as shown at the bottom of the next page. Since the first two terms are dealt with in (18) and (19), we focus on the last term in the numerator of (23). It expands to the expression in (24), as shown at the bottom of the next page.

For the second term of (22), we have the expression in (25), as shown at the bottom of the next page. With the same argument to above, we focus on the last term of the numerator in (25), which is expanded to the expression in (26), as shown at the bottom of the next page.

Next we derive the derivatives of $\mathcal{L}$ with respect to $\{\rho_k\}_{2\le k\le K}$

$$\frac{\partial}{\partial \rho_k}\mathcal{L} = \sum_{i=1}^{n}\frac{\partial}{\partial \rho_k}\log f(y_{i1},y_{i2}).$$

For this, we have

$$\frac{\partial}{\partial \rho_k}\log f(y_{i1},y_{i2}) = \frac{\pi_k\frac{\partial}{\partial \rho_k}\phi(y_{i1},y_{i2};\boldsymbol{\mu}_k,\boldsymbol{\Sigma}_k)}{f(y_{i1},y_{i2})}. \quad (27)$$

The numerator of (27) expands to the expression in (28), as shown at the bottom of the next page.

To derive the derivatives of $\mathcal{L}$ with respect to $\{v_{kj}\}_{2\le k\le K, j=1,2,3}$, we need to calculate the derivatives of σ_{kj}'s and ρ_k's with respect to v_{kj}'s. From $\sigma_{k1}^2 = v_{k1}^2$, we have

$$\frac{\partial\sigma_{k1}}{\partial v_{k1}} = \text{sign}(v_{k1}).$$

From $\sigma_{k2}^2 = v_{k2}^2 + v_{k3}^2$, we have

$$\begin{aligned}\frac{\partial\sigma_{k2}}{\partial v_{k2}} &= \frac{\partial}{\partial v_{k2}}(v_{k_2}^2+v_{k3}^2)^{1/2} = \frac{1}{2}(v_{k_2}^2+v_{k3}^2)^{-1/2}\cdot 2v_{k2}\\ &= \frac{v_{k2}}{\sigma_{k2}},\\ \frac{\partial\sigma_{k2}}{\partial v_{k3}} &= \frac{v_{k3}}{\sigma_{k2}}.\end{aligned}$$

From

$$\rho_k = \frac{v_{k1}v_{k2}}{\sigma_{k1}\sigma_{k2}} = \frac{v_{k1}v_{k2}}{|v_{k1}|\sqrt{v_{k2}^2+v_{k3}^2}} = \text{sign}(v_{k1})\frac{v_{k2}}{\sqrt{v_{k2}^2+v_{k3}^2}},$$

we have

$$\begin{aligned}\frac{\partial\rho_k}{\partial v_{k1}} &= 0,\\ \frac{\partial\rho_k}{\partial v_{k2}} &= \text{sign}(v_{k1})\frac{\sqrt{v_{k2}^2+v_{k3}^2} - v_{k2}^2(v_{k2}^2+v_{k3}^2)^{-1/2}}{v_{k2}^2+v_{k3}^2}\\ &= \text{sign}(v_{k1})\left(\frac{1}{\sigma_{k2}} - \frac{v_{k2}^2}{\sigma_{k2}^3}\right),\\ \frac{\partial\rho_k}{\partial v_{k3}} &= \text{sign}(v_{k1})\left(-\frac{v_{k2}v_{k3}}{\sigma_{k2}^3}\right).\end{aligned}$$

$$\begin{aligned}\frac{\partial}{\partial y_{ij}}\phi(y_{i1},y_{i2};\boldsymbol{\mu}_k,\boldsymbol{\Sigma}_k) &= \frac{\partial}{\partial y_{ij}}\frac{1}{2\pi\sigma_{k1}\sigma_{k2}\sqrt{1-\rho_k^2}}\exp\left(-\frac{1}{2(1-\rho_k^2)}\left\{\left(\frac{y_{i1}-\mu_{k1}}{\sigma_{k1}}\right)^2\right.\right.\\ &\quad\left.\left.-2\rho_k\frac{y_{i1}-\mu_{k1}}{\sigma_{k1}}\frac{y_{i2}-\mu_{k2}}{\sigma_{k2}}+\left(\frac{y_{i2}-\mu_{k2}}{\sigma_{k2}}\right)^2\right\}\right)\\ &= \phi(y_{i1},y_{i2};\boldsymbol{\mu}_k,\boldsymbol{\Sigma}_k)\left\{-\frac{1}{2(1-\rho_k^2)}\left(2\frac{y_{ij}-\mu_{kj}}{\sigma_{kj}^2}-2\rho_k\frac{y_{i\hat{j}}-\mu_{k\hat{j}}}{\sigma_{k1}\sigma_{k2}}\right)\right\}. \quad (19)\end{aligned}$$

$$\frac{\partial}{\partial \mu_{kj}}\phi(y_{i1},y_{i2};\boldsymbol{\mu}_k,\boldsymbol{\Sigma}_k) = \phi(y_{i1},y_{i2};\boldsymbol{\mu}_k,\boldsymbol{\Sigma}_k)\left\{-\frac{1}{2(1-\rho_k^2)}\left(-2\frac{y_{ij}-\mu_{kj}}{\sigma_{kj}^2}+2\rho_k\frac{y_{i\hat{j}}-\mu_{k\hat{j}}}{\sigma_{k1}\sigma_{k2}}\right)\right\}. \quad (20)$$

$$\begin{aligned}\frac{\partial}{\partial \mu_{kj}}\log\psi_j(y_{ij}) &= \frac{\frac{\partial}{\partial \mu_{kj}}\left\{\pi_1\phi(y_{ij})+\sum_{l=2}^{K}\pi_l\phi(y_{ij};\mu_{lj},\sigma_{lj}^2)\right\}}{\psi_j(y_{ij})}\\ &= \frac{\frac{\partial y_{ij}}{\partial \mu_{kj}}\frac{\partial}{\partial y_{ij}}\left\{\pi_1\phi(y_{ij})+\sum_{l=2}^{K}\pi_l\phi(y_{ij};\mu_{lj},\sigma_{lj}^2)\right\}+\pi_k\frac{\partial}{\partial \mu_{kj}}\phi(y_{ij};\mu_{kj},\sigma_{kj}^2)}{\psi_j(y_{ij})}. \quad (21)\end{aligned}$$

In sum, with the above equations, we have

$$\frac{\partial}{\partial v_{k1}}\mathcal{L} = \frac{\partial \sigma_{k1}}{\partial v_{k1}}\frac{\partial}{\partial \sigma_{k1}}\mathcal{L},$$
$$\frac{\partial}{\partial v_{k2}}\mathcal{L} = \frac{\partial \sigma_{k2}}{\partial v_{k2}}\frac{\partial}{\partial \sigma_{k2}}\mathcal{L} + \frac{\partial \rho_k}{\partial v_{k2}}\frac{\partial}{\partial \rho_k}\mathcal{L},$$
$$\frac{\partial}{\partial v_{k3}}\mathcal{L} = \frac{\partial \sigma_{k2}}{\partial v_{k3}}\frac{\partial}{\partial \sigma_{k2}}\mathcal{L} + \frac{\partial \rho_k}{\partial v_{k3}}\frac{\partial}{\partial \rho_k}\mathcal{L}.$$

Finally, we derive the derivatives of $\mathcal{L}$ with respect to $\{\alpha_k\}_{k=1}^K$. To this end, we first derive the derivatives of $\mathcal{L}$ with respect to $\{\pi_k\}_{k=1}^K$

$$\frac{\partial}{\partial \pi_k}\mathcal{L} = \sum_{i=1}^{n}\left(\frac{\partial}{\partial \pi_k}\log f(y_{i1}, y_{i2}) - \frac{\partial}{\partial \pi_k}\log \psi_j(y_{ij})\right). \quad (29)$$

For the first term of (29), we obtain the expression in (30), as shown at the bottom of the page. For the second term of (29),

$$\frac{\partial}{\partial \sigma_{kj}}\log f(y_{i1}, y_{i2}) = \frac{\frac{\partial y_{ij}}{\partial \sigma_{kj}}\frac{\partial}{\partial y_{ij}}\left\{\pi_1\phi(y_{i1}, y_{i2}; \mathbf{0}, \mathbf{I}_2) + \sum_{l=2}^{K}\pi_l\phi(y_{i1}, y_{i2}; \boldsymbol{\mu}_l, \boldsymbol{\Sigma}_l)\right\} + \pi_k\frac{\partial}{\partial \sigma_{kj}}\phi(y_{i1}, y_{i2}; \boldsymbol{\mu}_k, \boldsymbol{\Sigma}_k)}{f(y_{i1}, y_{i2})}. \quad (23)$$

$$\begin{aligned}\frac{\partial}{\partial \sigma_{kj}}\phi(y_{i1}, y_{i2}; \boldsymbol{\mu}_k, \boldsymbol{\Sigma}_k) &= \frac{\partial}{\partial \sigma_{kj}}\frac{1}{2\pi\sigma_{k1}\sigma_{k2}\sqrt{1-\rho_k^2}}\exp\Bigg(-\frac{1}{2(1-\rho_k^2)}\Bigg\{\left(\frac{y_{i1}-\mu_{k1}}{\sigma_{k1}}\right)^2 - 2\rho_k\frac{y_{i1}-\mu_{k1}}{\sigma_{k1}}\frac{y_{i2}-\mu_{k2}}{\sigma_{k2}} \\ &\quad + \left(\frac{y_{i2}-\mu_{k2}}{\sigma_{k2}}\right)^2\Bigg\}\Bigg) \\ &= \phi(y_{i1}, y_{i2}; \boldsymbol{\mu}_k, \boldsymbol{\Sigma}_k)\left(-\frac{1}{\sigma_{kj}}\right) + \phi(y_{i1}, y_{i2}; \boldsymbol{\mu}_k, \boldsymbol{\Sigma}_k)\left(-\frac{1}{2(1-\rho_k^2)}\right)\Bigg\{-\frac{2}{\sigma_{kj}}\left(\frac{y_{ij}-\mu_{kj}}{\sigma_{kj}^2}\right)^2 \\ &\quad + \frac{2\rho_k}{\sigma_{kj}}\frac{y_{i1}-\mu_{k1}}{\sigma_{k1}}\frac{y_{i2}-\mu_{k2}}{\sigma_{k2}}\Bigg\} \\ &= -\phi(y_{i1}, y_{i2}; \boldsymbol{\mu}_k, \boldsymbol{\Sigma}_k)\left(\frac{1}{\sigma_{kj}}\right)\left[1 + \frac{1}{(1-\rho_k^2)}\left\{-\left(\frac{y_{ij}-\mu_{kj}}{\sigma_{kj}^2}\right)^2 + \rho_k\left(\frac{y_{i1}-\mu_{k1}}{\sigma_{k1}}\right)\left(\frac{y_{i2}-\mu_{k2}}{\sigma_{k2}}\right)\right\}\right]. \end{aligned} \quad (24)$$

$$\frac{\partial}{\partial \sigma_{kj}}\log \psi_j(y_{ij}) = \frac{\frac{\partial y_{ij}}{\partial \sigma_{kj}}\frac{\partial}{\partial y_{ij}}\left\{\pi_1\phi(y_{ij}) + \sum_{l=2}^{K}\pi_l\phi(y_{ij}; \mu_{lj}, \sigma_{lj}^2)\right\} + \pi_k\frac{\partial}{\partial \sigma_{kj}}\phi(y_{ij}; \mu_{kj}, \sigma_{kj}^2)}{\psi_j(y_{ij})}. \quad (25)$$

$$\begin{aligned}\frac{\partial}{\partial \sigma_{kj}}\phi(y_{ij}; \mu_{kj}, \sigma_{kj}^2) &= \phi(y_{ij}; \mu_{kj}, \sigma_{kj}^2)\left(-\frac{1}{\sigma_{kj}}\right) + \phi(y_{ij}; \mu_{kj}, \sigma_{kj}^2)\frac{\partial}{\partial \sigma_{kj}}\left\{-\frac{1}{2}\left(\frac{y_{ij}-\mu_{kj}}{\sigma_{kj}}\right)^2\right\} \\ &= -\phi(y_{ij}; \mu_{kj}, \sigma_{kj}^2)\frac{1}{\sigma_{kj}}\left\{1 - \left(\frac{y_{ij}-\mu_{kj}}{\sigma_{kj}}\right)^2\right\}. \end{aligned} \quad (26)$$

$$\begin{aligned}&\frac{\partial}{\partial \rho_k}\phi(y_{i1}, y_{i2}; \boldsymbol{\mu}_k, \boldsymbol{\Sigma}_k) \\ &= \phi(y_{i1}, y_{i2}; \boldsymbol{\mu}_k, \boldsymbol{\Sigma}_k)\frac{\rho_k}{1-\rho_k^2} \\ &\quad + \phi(y_{i1}, y_{i2}; \boldsymbol{\mu}_k, \boldsymbol{\Sigma}_k)\left[-\frac{\rho_k}{(1-\rho_k^2)^2}\left\{\left(\frac{y_{i1}-\mu_{k1}}{\sigma_{k1}}\right)^2 + \left(\frac{y_{i2}-\mu_{k2}}{\sigma_{k2}}\right)^2\right\} + \frac{1+\rho_k^2}{(1-\rho_k^2)^2}\frac{y_{i1}-\mu_{k1}}{\sigma_{k1}}\frac{y_{i2}-\mu_{k2}}{\sigma_{k2}}\right] \\ &= \frac{\phi(y_{i1}, y_{i2}; \boldsymbol{\mu}_k, \boldsymbol{\Sigma}_k)}{1-\rho_k^2}\left[\rho_k - \frac{\rho_k}{1-\rho_k^2}\left\{\left(\frac{y_{i1}-\mu_{k1}}{\sigma_{k1}}\right)^2 + \left(\frac{y_{i2}-\mu_{k2}}{\sigma_{k2}}\right)^2\right\} + \frac{1+\rho_k^2}{1-\rho_k^2}\frac{y_{i1}-\mu_{k1}}{\sigma_{k1}}\frac{y_{i2}-\mu_{k2}}{\sigma_{k2}}\right]. \end{aligned} \quad (28)$$

$$\frac{\partial}{\partial \pi_k}\log f(y_{i1}, y_{i2}) = \frac{\frac{\partial y_{i1}}{\partial \pi_k}\frac{\partial}{\partial y_{i1}}f(y_{i1}, y_{i2}) + \frac{\partial y_{i2}}{\partial \pi_k}\frac{\partial}{\partial y_{i2}}f(y_{i1}, y_{i2}) + \mathbf{1}_{\{k=1\}}\phi(y_1, y_2; \mathbf{0}, \mathbf{I}_2) + \mathbf{1}_{\{k\neq 1\}}\phi(y_1, y_2; \boldsymbol{\mu}_k, \boldsymbol{\Sigma}_k)}{f(y_{i1}, y_{i2})} \quad (30)$$

$$\frac{\partial}{\partial \pi_k}\log \psi_j(y_{ij}) = \frac{\frac{\partial y_{ij}}{\partial \pi_k}\frac{\partial}{\partial y_{ij}}\psi_j(y_{ij}) + \mathbf{1}_{\{k=1\}}\phi(y_j) + \mathbf{1}_{\{k\neq 1\}}\phi(y_j; \mu_{kj}, \sigma_{kj}^2)}{\psi_j(y_{ij})}. \quad (31)$$

we obtain the expression in (31), as shown at the bottom of the previous page. Note from (14) that

$$\frac{\partial \pi_k}{\partial \alpha_k} = \frac{\exp(\alpha_k)\left(\sum_{k'=1}^{K}\exp(\alpha_{k'})\right) - (\exp(\alpha_k))^2}{\left(\sum_{k'=1}^{K}\exp(\alpha_{k'})\right)^2}$$
$$= \pi_k(1-\pi_k),$$
$$\frac{\partial \pi_l}{\partial \alpha_k} = \exp(\alpha_l)\left(-\frac{\exp(\alpha_l)}{\left(\sum_{k'=1}^{K}\exp(\alpha_{k'})\right)^2}\right) = -\pi_l\pi_k.$$

In sum, we have

$$\frac{\partial}{\partial \alpha_k}\mathcal{L} = \sum_{l=1}^{K}\frac{\partial \pi_l}{\partial \alpha_k}\frac{\partial}{\partial \pi_l}\mathcal{L} = \sum_{l=1}^{K}\pi_k(\mathbf{1}_{\{l=k\}} - \pi_l)\frac{\partial}{\partial \pi_l}\mathcal{L}.$$

REFERENCES

[1] G. Ancans, V. Bobrovs, A. Ancans, and D. Kalibatiene, "Spectrum considerations for 5G mobile communication systems," *Proc. Comput. Sci.*, vol. 104, pp. 509–516, May 2017, doi: 10.1016/j.procs.2017.01.166.

[2] J. Xing, Z. Zhang, Q. Liu, W. Zhan, S. Shao, and K. Lin, "5G radio-frequency design," in *5G NR Enhancements From R15 to R16*, J. Shen, Z. Du, Z. Zhang, N. Yang, and H. Tang, Eds., Amsterdam, The Netherlands: Elsevier, 2022.

[3] H. Holma and A. Toskala, "Introduction," in *LTE for UMTS : Evolution to LTE-Advanced*. Hoboken, NJ, USA: Wiley, 2011.

[4] J. Um, I. Kim, and S. Park, "Implementation of platform for long-term evolution cell perspective resource utilization analysis," *ETRI J.*, vol. 43, no. 2, pp. 232–245, Apr. 2021, doi: 10.4218/etrij.2019-0475.

[5] J. Choi and S. Im, "Multivariate kernel density estimation performance in detecting abnormalities in three-phase induction motors with a focus on optimizing kernel and bandwidth," *IEEE Access*, vol. 12, pp. 138594–138609, 2024, doi: 10.1109/ACCESS.2024.3465497.

[6] M. P. Deisenroth, A. A. Faisal, and C. S. Ong, *Mathematics for Machine Learning*. Cambridge, U.K.: Cambridge Univ. Press, 2020.

[7] A. Sklar, "Fonctions de rèpartition á *n* dimensions et leurs marges," *Publ. Inst. Statist. Univ. Paris*, vol. 8, no. 3, pp. 229–231, 1959.

[8] C. Czado and T. Nagler, "Vine copula based modeling," *Annu. Rev. Statist. Appl.*, vol. 9, no. 1, pp. 453–477, Mar. 2022, doi: 10.1146/annurev-statistics-040220-101153.

[9] D. Kurowicka and H. Joe, *Dependence Modeling: Vine Copula Handbook*. Singapore: World Scientific, 2011.

[10] T. Bedford and R. M. Cooke, "Vines—A new graphical model for dependent random variables," *Ann. Statist.*, vol. 30, no. 4, pp. 1031–1068, Aug. 2002, doi: 10.1214/aos/1031689016.

[11] O. Morales-Nápoles, R. Cooke, and D. Kurowicka, "About the number of vines and regular vines on *n* nodes," Delft Inst. Appl. Math., Delft Univ. Technol., The Netherlands, Tech. Rep., 2010.

[12] J. Dißmann, E. C. Brechmann, C. Czado, and D. Kurowicka, "Selecting and estimating regular vine copulae and application to financial returns," *Comput. Statist. Data Anal.*, vol. 59, pp. 52–69, Mar. 2013, doi: 10.1016/j.csda.2012.08.010.

[13] L. Gruber and C. Czado, "Sequential Bayesian model selection of regular vine copulas," *Bayesian Anal.*, vol. 10, no. 4, pp. 937–963, Dec. 2015, doi: 10.1214/14-ba930.

[14] L. F. Gruber and C. Czado, "Bayesian model selection of regular vine copulas," *Bayesian Anal.*, vol. 13, no. 4, pp. 1111–1135, Dec. 2018, doi: 10.1214/17-ba1089.

[15] Y. Sun, A. Cuesta-Infante, and K. Veeramachaneni, "Learning vine copula models for synthetic data generation," in *Proc. AAAI*, 2019, pp. 5049–5057, doi: 10.1609/aaai.v33i01.33015049.

[16] A. Mitra, "Adapting the regulation of spectrum and telecom networks to 5G technology—A cross country analysis," in *Proc. Int. Work. Conf. Transf. Diffusion IT*, 2023, pp. 107–125.

[17] A. Tewari, M. J. Giering, and A. Raghunathan, "Parametric characterization of multimodal distributions with non-Gaussian modes," in *Proc. IEEE 11th Int. Conf. Data Mining Workshops*, Dec. 2011, pp. 286–292.

[18] R. B. Nelsen, *An Introduction to Copulas*, 2nd ed., New York, NY, USA: Springer, 2006.

[19] H. Joe, *Dependence Modeling With Copulas*. Boca Raton, FL, USA: CRC Press, 2014.

[20] D. Kurowicka and R. Cooke, *Uncertainty Analysis With High Dimensional Dependence Modelling*. Hoboken, NJ, USA: Wiley, 2006.

[21] A. E. Bilgrau, P. S. Eriksen, J. G. Rasmussen, H. E. Johnsen, K. Dybkaer, and M. Boegsted, "GMCM: Unsupervised clustering and meta-analysis using Gaussian mixture copula models," *J. Stat. Softw.*, vol. 70, no. 2, pp. 1–23, Apr. 2016, doi: 10.18637/jss.v070.i02.

[22] S. R. Kasa and V. Rajan, "Improved inference of Gaussian mixture copula model for clustering and reproducibility analysis using automatic differentiation," *Econometrics Statist.*, vol. 22, pp. 67–97, Apr. 2022, doi: 10.1016/j.ecosta.2021.08.010.

[23] G. Geenens, "Probit transformation for kernel density estimation on the unit interval," *J. Amer. Stat. Assoc.*, vol. 109, no. 505, pp. 346–358, Jan. 2014, doi: 10.1080/01621459.2013.842173.

[24] C. M. Bishop, *Pattern Recognition and Machine Learning*. New York, NY, USA: Springer, 2006.

[25] Q. Li, J. B. Brown, H. Huang, and P. J. Bickel, "Measuring reproducibility of high-throughput experiments," *Ann. Appl. Statist.*, vol. 5, no. 3, pp. 1752–1779, Sep. 2011, doi: 10.1214/11-aoas466.

[26] J. Yoon, Y. Kim, H. Kwon, and S. Park, "Data-driven active session identification for LTE user-perceived QoS analysis," *Comput. Netw.*, vol. 258, Feb. 2025, Art. no. 111042, doi: 10.1016/j.comnet.2025.111042.

[27] D. P. Kingma and J. Ba, "Adam: A method for stochastic optimization," 2014, *arXiv:1412.6980*.

[28] Z. Ma and A. Leijon, "Bayesian estimation of beta mixture models with variational inference," *IEEE Trans. Pattern Anal. Mach. Intell.*, vol. 33, no. 11, pp. 2160–2173, Nov. 2011, doi: 10.1109/TPAMI.2011.63.

[29] T. Hastie, R. Tibshirani, and J. Friedman, "Undirected graphical models," in *The Elements of Statistical Learning: Data Mining, Inference, and Prediction*, 2nd ed., Berlin, Germany: Springer, 2009, pp. 625–648.

[30] C. Durkan, A. Bekasov, I. Murray, and G. Papamakarios, "Neural spline flows," in *Proc. 33rd Int. Conf. Neural Inf. Process. Syst.*, 2019, pp. 7511–7522.

[31] G. Fasano and A. Franceschini, "A multidimensional version of the Kolmogorov–Smirnov test," *Monthly Notices Roy. Astronomical Soc.*, vol. 225, no. 1, pp. 155–170, Mar. 1987, doi: 10.1093/mnras/225.1.155.

[32] R. Xiao, P. Combeau, and L. Aveneau, "Monte Carlo integration with efficient importance sampling for underwater wireless optical communication simulation," *IEEE Access*, vol. 13, pp. 73652–73670, 2025, doi: 10.1109/ACCESS.2025.3564070.

[33] M. C. Jones and I. Koch, "Dependence maps: Local dependence in practice," *Statist. Comput.*, vol. 13, no. 3, pp. 241–255, Aug. 2003, doi: 10.1023/a:1024270700807.

[34] S. Park, M. Agiwal, H. Kwon, and H. Jin, "An evaluation methodology for spectrum usage in LTE—A networks: Traffic volume and resource utilization perspective," *IEEE Access*, vol. 7, pp. 67863–67873, 2019, doi: 10.1109/ACCESS.2019.2918646.

[35] H. S. Jang, H. Lee, H. Kwon, and S. Park, "Deep learning-based prediction of resource block usage rate for spectrum saturation diagnosis," *IEEE Access*, vol. 9, pp. 59703–59714, 2021, doi: 10.1109/ACCESS.2021.3073670.

YUNBAE KIM received the B.S. degree and the B.Sc. and Ph.D. degrees in mathematical sciences from Korea Advanced Institute of Science and Technology (KAIST), Daejeon, South Korea, in 2009 and 2015, respectively. Since November 2015, he has been with the Electronics and Telecommunications Research Institute (ETRI), Daejeon. His research interests include performance evaluation and optimization of wireless communication networks.

JONGHUN YOON received the B.S. degree in mathematics from Korea University, Seoul, South Korea, in 2012, and the M.S. and Ph.D. degrees in mathematical sciences from Korea Advanced Institute of Science and Technology (KAIST), Daejeon, South Korea, in 2014 and 2018, respectively. From 2018 to March 2019, he was with Data Analytics Laboratory within AI Center at Samsung Research, Seoul. Since April 2019, he has been with Radio Research Division with Electronics and Telecommunications Research Institute (ETRI), Daejeon. His research interests include the performance evaluation and optimization of communication networks, as well as data analytics for spectrum management.

HYEYEON KWON received the B.S. degree in computer science and statistics from Chungnam National University, Daejeon, Republic of Korea, in 1990, and the M.S. and Ph.D. degrees in computer science in 2000 and 2006, respectively. She is currently a Principal Researcher with the Electronics and Telecommunications Research Institute, Daejeon. Her current research interests include mobile communication networks and data analysis for spectrum management.

SEUNGKEUN PARK (Member, IEEE) received the B.S. and M.S. degrees in applied statistics from Korea University, Seoul, Republic of Korea, in 1991 and 1993, respectively, and the Ph.D. degree in information communication engineering from the University of Chungbuk, Cheongju-si, Republic of Korea, in 2004. He is currently a Principal Researcher with the Electronics and Telecommunications Research Institute, Daejeon, Republic of Korea. His current research interests include communication theory and spectrum management.